PROCEEDINGS A

rspa.royalsocietypublishing.org

Research

Cite this article: Liu K, Paulino GH. 2017 Nonlinear mechanics of non-rigid origami: an efficient computational approach. *Proc. R. Soc. A* **473**: 20170348.
http://dx.doi.org/10.1098/rspa.2017.0348

Received: 17 May 2017
Accepted: 5 September 2017

Subject Areas:
structural engineering, mechanical engineering, mechanics

Keywords:
origami, bar-and-hinge model, nonlinear analysis, elastic deformations, large displacement, large deformation

Author for correspondence:
G. H. Paulino
e-mail: paulino@gatech.edu

†Dedicated to the memory of Prof. Richard H. Gallagher (1927–1997).

Electronic supplementary material is available online at https://dx.doi.org/10.6084/m9.figshare.c.3887758.

THE ROYAL SOCIETY PUBLISHING

Nonlinear mechanics of non-rigid origami: an efficient computational approach†

K. Liu and G. H. Paulino

School of Civil and Environmental Engineering, Georgia Institute of Technology, Atlanta, GA 30332, USA

GHP, 0000-0002-3493-6857

Origami-inspired designs possess attractive applications to science and engineering (e.g. deployable, self-assembling, adaptable systems). The special geometric arrangement of panels and creases gives rise to unique mechanical properties of origami, such as reconfigurability, making origami designs well suited for tunable structures. Although often being ignored, origami structures exhibit additional soft modes beyond rigid folding due to the flexibility of thin sheets that further influence their behaviour. Actual behaviour of origami structures usually involves significant geometric nonlinearity, which amplifies the influence of additional soft modes. To investigate the nonlinear mechanics of origami structures with deformable panels, we present a structural engineering approach for simulating the nonlinear response of non-rigid origami structures. In this paper, we propose a fully nonlinear, displacement-based implicit formulation for performing static/quasi-static analyses of non-rigid origami structures based on 'bar-and-hinge' models. The formulation itself leads to an efficient and robust numerical implementation. Agreement between real models and numerical simulations demonstrates the ability of the proposed approach to capture key features of origami behaviour.

1. Introduction

Origami concepts have been used in many fields of science and engineering—applications include, for example, deployable space structures [1,2], assembly of complex architectures [3,4] and design of functional metamaterials [3,5]. Various approaches have been proposed in order to understand large deformations of origami structures including the folding process. Following rigid origami assumption, Belcastro & Hull [6]

developed an affine transformation map to describe the folding of a single vertex origami. Tachi [7] extended this idea to simulate the folding of complex origami sheets with arbitrary patterns. Wu & You [8] presented a quaternion-based formulation for rigid origami simulation. For some particular patterns that can be assembled with repeated unit cells, such as the Miura-ori and its derivatives [9,10], closed-form equations were derived to describe the entire folding process. However, the aforementioned approaches, based on purely geometric considerations, are applicable only to rigid origami, i.e. they assume that all the panels in an origami structure are rigid surfaces.

Owing to the flexibility of thin sheets, origami structures actually gain additional degrees of freedom that come from bending, stretching and shearing of panels. Thus, rigid origami simulations are not sufficient to reflect the actual behaviour of a physical origami structure. Direct modelling of origami structures is possible by means of finite-element (FE) analysis with shell elements [11]. It provides detailed information such as stress distribution, but also requires a time-consuming cycle for both modelling and computing, including pre- and post-processing [12–15]. Shell elements are typically computationally expensive and have issues associated with numerical artefacts, such as shear locking and membrane locking [16–18]. As the thickness of the origami panels decreases, specialized approaches are needed [19]. In addition, local instabilities may influence the convergence of the analysis on the global scale. In some instances, the approximate global behaviour of an origami structure is of more interest than high-resolution local deformations. In such instances, a simpler and specialized analysis tool is required and should be able to track global deformations of origami structures, while being less sensitive to local instabilities.

A commonly adopted technique to simplify the analysis of origami structures consists of representing an origami structure with a reduced degree-of-freedom model. Resch & Christiansen [20] exploited linear elastic rotational hinges for the folding creases, and modelled each panel using a plane stress element. Kumar & Pellegrino [21] used triangulated truss mechanisms to represent origami structures for kinematic path analyses. Evans *et al.* [22] ignored in-plane deformations, but introduced extra diagonal bending lines within each panel to reflect the bending of panels. Tachi [23] used a similar simplification while adopting an iterative strategy to handle large developable transformations. Such simplification was also adopted by Brunck [24].

Schenk & Guest [25,26] proposed a bar-and-hinge model, where an origami sheet is triangulated to a truss framework with constrained rotational hinges. The basic idea of the model is shown in figure 1, considering the Miura-ori as an example. Bars are placed along straight fold lines, and across panels for in-plane stiffness. The rotational hinges are along bars connecting panels to model folding of creases, and along bars across panels to model bending of panels. Such simplified representation is effective for origami structures with quadrilateral panels [27,28]. A linear elastic formulation in association with the bar-and-hinge model was derived to analyse infinitesimal deformations of origami [25]. Both the bars and the rotations are assigned with constant stiffness. The same discretization scheme was adopted by Wei *et al.* [29] to simulate bending of the Miura-ori, based on an explicit formulation through time integration without construction of stiffness matrices. Artificial damping is needed to force the structure to come to rest, which is a strategy usually used in computer animation to simulate soft surfaces such as cloth [30]. In the bar-and-hinge model, triangular panels may not need to be divided—previous work by Guest & Pellegrino [31] showed the effectiveness of such bar-and-hinge simplification in modelling a triangulated cylindrical pattern.

The structural analysis formulation proposed by Schenk & Guest [25] captures the global deformation modes of various origami structures well. Based on reference [25], Fuchi *et al.* [32,33] implemented the linear bar-and-hinge model as the structural analysis module for topology optimization of origami structures. Filipov *et al.* [3] used a variation of the model with enriched discretization to analyse mechanical properties of the so-called zipper origami tube. Notably, the theory associated to the bar-and-hinge simplification has only been developed for infinitesimal deformations; however, for many applications, the attractive feature of origami is its ability to undergo large configurational transformations. Therefore, there is a need for a robust and simple

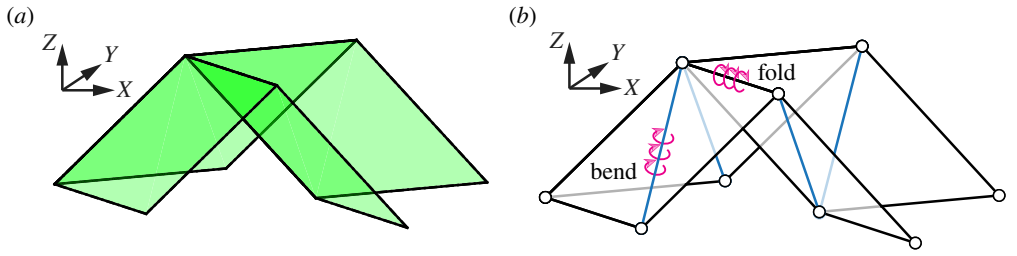

Figure 1. (*a*) The Miura-ori unit cell. (*b*) The bar-and-hinge model for a unit cell of Miura-ori. The black bars represent creases and boundaries of the origami and the blue bars are added to model in-plane and out-of-plane deformations of the panels. (Online version in colour).

approach that can simulate large deformations and displacements of origami structures—this is the focus of the present work.

In this paper, we propose a general nonlinear formulation for structural analysis of origami structures associated with arbitrary bar-and-hinge models. The formulation is displacement-based, and considers both geometric and material nonlinearities, building up a fully nonlinear framework for large displacement and large deformation analyses of origami structures. It is more than a straightforward extension of the existing linear formulation [25]. For instance, geometric nonlinearity arising from large rotations must be carefully addressed to avoid singularities which usually do not arise under infinitesimal deformation. The proposed formulation is implicit, which enforces equilibrium at each converged incremental step; thus, it is more suitable for static/quasi-static analysis compared to explicit approaches by direct time integration.

The idealization of this paper is motivated by the pioneering work of Prof. Richard H. Gallagher on matrix structural analysis [34–36] and FE [37]. His work paved the way for many developments in the field and thus our numerical formulation of nonlinear mechanics for non-rigid origami is inspired from the fundamental work by Gallagher and his colleagues. The remainder of this paper is organized as follows. Section 2 presents the derivation and associated components of the formulation. Special attention is paid to the geometric terms in the tangent stiffness matrix. Section 3 addresses the solution scheme for the nonlinear formulation. Section 4 provides numerical examples of origami simulations using the nonlinear bar-and-hinge model. We compare numerical simulations with paper-made models to manifest that the proposed approach is able to capture key features in the deformation process of origami structures. Conclusions are drawn in §5. Three appendices supplement the paper, including a nomenclature. The proposed formulation is implemented by the 'MERLIN' software written in MATLAB [38], which is attached as electronic supplementary material.

2. Nonlinear formulation for bar-and-hinge models

From the aforementioned discussion, we adopt a potential energy approach to formulate the nonlinear bar-and-hinge model. This is followed by the FE implementation of bar elements and rotational spring elements. The treatment of finite rotations is a major aspect of the present work because the classical approach of using trigonometric functions to derive internal force vectors and tangent stiffness matrices fails due to singularities in the gradients of those functions. Thus, we propose enhanced formulae based on distance vectors and functions which are free of singularities in their gradients. Next, we provide the constitutive relationships for bars and rotational springs. The relevant aspect there is that we transfer the problem of (local) contact to the constitutive model of the rotational springs. These remarks are elaborated upon below.

(a) Principle of stationary potential energy

The potential energy of the bar-and-hinge system, which is assumed to be conservative, is only a function of the current configuration, independent of deformation history. Thus, we use the principle of stationary potential energy [39] to derive the equilibrium condition and tangent stiffness matrix, while accounting for both material (constitutive relationship) and geometric nonlinearities. We describe the kinematics by the total Lagrangian approach, taking reference to the initial configuration. The potential energy of the system comprises of internal strain energy (or stored energy) and external (load) work (V_{ext}). We separate the strain energy into two components: one stored in the bar elements (U_{bar}) and the other stored in the rotational springs (U_{spr}). Thus, we have the following expression for the total potential energy:

$$\Pi = U_{\text{bar}} + U_{\text{spr}} - V_{\text{ext}}. \tag{2.1}$$

The equilibrium of the system is reached when the potential energy is stationary, that is, the first variation of the total potential energy becomes zero. Considering the origami discretization given by the bar-and-hinge model, we obtain the directional derivative of the total potential energy with respect to finite degrees of freedom as follows:

$$\mathcal{D}\Pi\delta\mathbf{v} = \delta\mathbf{v}^{\mathrm{T}}\mathbf{R} = 0. \tag{2.2}$$

The term $\mathcal{D}$ denotes the directional derivative operator, $\delta\mathbf{v}$ refers to a virtual displacement and $\mathbf{R}$ denotes the residual force vector. For clarity, let us denote the vector $\mathbf{X}$ as the collection of nodal coordinates in the undeformed configuration, and $\mathbf{x}$ as nodal coordinates in the deformed configuration. The (total) displacement vector $\mathbf{u}$ is defined as $\mathbf{u} = \mathbf{x} - \mathbf{X}$. The nonlinear equilibrium equation can be symbolically assembled as follows:

$$\mathbf{R}(\mathbf{u}) = \mathbf{T}_{\text{bar}}(\mathbf{u}) + \mathbf{T}_{\text{spr}}(\mathbf{u}) - \mathbf{F}(\mathbf{u}) = \mathbf{0}. \tag{2.3}$$

The vector $\mathbf{F}$ contains the forces applied to the nodes of the bar-and-hinge system, and $\mathbf{T}$ denotes the internal force vector. Linearization of the equilibrium equation (equation (2.3)) provides second-order approximation about the total potential energy, which leads to the tangent stiffness matrix, as shown below:

$$\mathcal{D}\mathbf{R}\delta\mathbf{u} = \mathbf{K}\delta\mathbf{u}, \tag{2.4}$$

where $\delta\mathbf{u}$ refers to a small nodal displacement perturbation. Similarly, the tangent stiffness matrix can be decomposed into two contributing terms:

$$\mathbf{K}(\mathbf{u}) = \mathbf{K}_{\text{bar}}(\mathbf{u}) + \mathbf{K}_{\text{spr}}(\mathbf{u}). \tag{2.5}$$

We elaborate on the internal force vectors and tangent stiffness matrices of each component in the following subsections. The goal is to assemble the internal force vector and tangent stiffness matrix of the whole structure.

(b) Implementation of bar elements

We have adopted hyperelasticity as the basis for our constitutive models in the paper because it provides a general framework that is able to represent a wider variety of constitutive behaviours than traditional linear elasticity (adopted in the original bar-and-hinge model). For many materials, linear elastic models do not accurately describe the observed material behaviour and thus hyperelasticity provides a means of modelling the stress–strain behaviour of such materials—this is helpful to capture the actual behaviour of origami sheets made with different materials (such as composites). For instance, we can easily consider materials with different compression and tension stiffness. In addition, the linear elastic constitutive model is not physical under large deformation, which could occur when an origami sheet has high in-plane compliance. In the worst scenario, negative principal stretch could happen with a linear elastic constitutive relationship, leading to unphysical response.

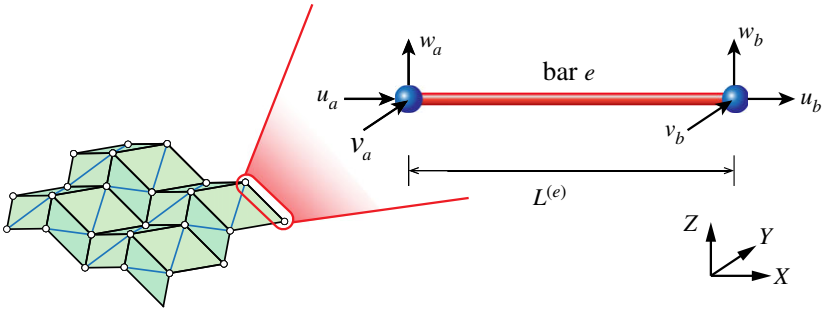

Figure 2. Components of a bar element, which is part of an origami assemblage. (Online version in colour.)

The constitutive relationship of a hyperelastic material is governed by a strain energy density function W [40]. This function is expressed in terms of the Green-Lagrange strain tensor $\boldsymbol{E}$ and its energy conjugate second Piola–Kirchhoff (P-K) stress tensor $\boldsymbol{S}$. We consider linear shape functions for the bar element and write the strain energy function as a function of nodal displacements. This FE formulation for nonlinear truss analysis has been extensively studied in previous literature [39,41], and here it is adapted to origami assemblages as part of the proposed nonlinear bar-and-hinge model. Below we summarize the FE formulation for bar elements using the matrix notation as adopted in this paper.

Let us assume that the bar element is described in its local coordinates, as shown in figure 2. We denote the area of one bar element as $A^{(e)}$, which is assumed to be constant along the longitudinal direction. The stored energy of a bar element is given by

$$U^{(e)}_{\text{bar}} = \int_0^{L^{(e)}} WA^{(e)}\,\mathrm{d}X. \tag{2.6}$$

Because bar elements are one dimensional, we only need to consider one component per stress tensor and strain tensor. Considering a linear shape function, we obtain the one-dimensional Green-Lagrange strain E_X as a function of the nodal displacements $\mathbf{u}^{(e)}$ [39,41]:

$$E_X = \mathbf{B}_1\mathbf{u}^{(e)} + \tfrac{1}{2}\mathbf{u}^{(e)\mathrm{T}}\mathbf{B}_2\mathbf{u}^{(e)}, \tag{2.7}$$

where $\mathbf{u}^{(e)} = [u_a, v_a, w_a, u_b, v_b, w_b]^{\mathrm{T}}$ (figure 2). The vector $\mathbf{B}_1$ is given by

$$\mathbf{B}_1 = \frac{1}{L^{(e)}}[-\mathbf{e}_1 \quad \mathbf{e}_1], \tag{2.8}$$

where $\mathbf{e}_1 = [1, 0, 0]$. The matrix $\mathbf{B}_2$ is

$$\mathbf{B}_2 = \frac{1}{(L^{(e)})^2}\begin{bmatrix} \boldsymbol{I}_{3\times3} & -\boldsymbol{I}_{3\times3} \\ -\boldsymbol{I}_{3\times3} & \boldsymbol{I}_{3\times3} \end{bmatrix}. \tag{2.9}$$

The matrix $\boldsymbol{I}_{3\times3}$ is the identity matrix of size 3 by 3. Substituting equation (2.7) into the gradient of equation (2.6), we obtain the internal force vector $\mathbf{T}^{(e)}_{\text{bar}}$ for a bar element e [39,41] as follows:

$$\mathbf{T}^{(e)}_{\text{bar}} = S_X A^{(e)} L^{(e)}(\mathbf{B}_1^{\mathrm{T}} + \mathbf{B}_2\mathbf{u}^{(e)}), \tag{2.10}$$

where S_X refers to the one-dimensional (assuming X direction) component of the second P-K stress tensor. Linearization of the internal force vector leads to the component tangent stiffness matrix, which is given by

$$\mathbf{K}^{(e)}_{\text{bar}} = CA^{(e)}L^{(e)}(\mathbf{B}_1^{\mathrm{T}} + \mathbf{B}_2\mathbf{u}^{(e)})(\mathbf{B}_1^{\mathrm{T}} + \mathbf{B}_2\mathbf{u}^{(e)})^{\mathrm{T}} + S_X A^{(e)} L^{(e)}\mathbf{B}_2. \tag{2.11}$$

The term C is the one-dimensional tangent modulus defined as

$$C = \frac{\partial S_X}{\partial E_X}. \tag{2.12}$$

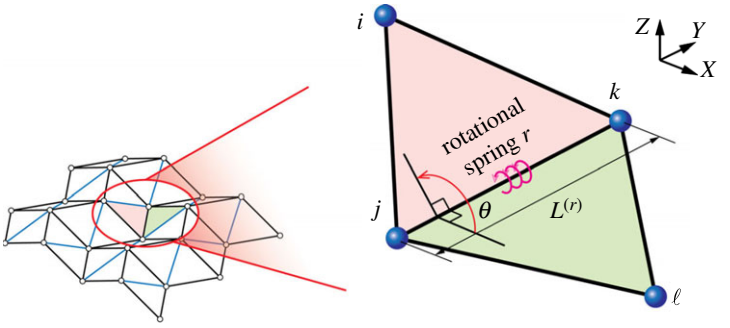

Figure 3. Components of a rotational spring element, which is part of an origami assemblage. (Online version in colour.)

Expanding the terms of the symmetric tangent stiffness matrix, we can recognize that $\mathbf{K}_{\text{bar}}^{(e)}$ is a summation of several matrices as follows:

$$\mathbf{K}_{\text{bar}}^{(e)} = \mathbf{K}_E^{(e)} + \mathbf{K}_1^{(e)} + \mathbf{K}_2^{(e)} + \mathbf{K}_G^{(e)}, \tag{2.13}$$

where

$$\mathbf{K}_E^{(e)} = CA^{(e)}L^{(e)}\mathbf{B}_1^{\mathrm{T}}\mathbf{B}_1, \tag{2.14}$$

$$\mathbf{K}_1^{(e)} = CA^{(e)}L^{(e)}((\mathbf{B}_2\mathbf{u}^{(e)})\mathbf{B}_1 + \mathbf{B}_1^{\mathrm{T}}(\mathbf{B}_2\mathbf{u}^{(e)})^{\mathrm{T}}), \tag{2.15}$$

$$\mathbf{K}_2^{(e)} = CA^{(e)}L^{(e)}(\mathbf{B}_2\mathbf{u}^{(e)})(\mathbf{B}_2\mathbf{u}^{(e)})^{\mathrm{T}} \tag{2.16}$$

and

$$\mathbf{K}_G^{(e)} = S_X A^{(e)}L^{(e)}\mathbf{B}_2. \tag{2.17}$$

The matrix $\mathbf{K}_E^{(e)}$ is the linear stiffness matrix, $\mathbf{K}_G^{(e)}$ is the geometric stiffness matrix and $(\mathbf{K}_1^{(e)} + \mathbf{K}_2^{(e)})$ forms the initial displacement matrix. To assemble the global stiffness matrix, the element stiffness matrix needs to be transformed from its local coordinates to the global coordinates. The resultant matrix, after transformation, can be derived explicitly, where $\mathbf{B}_2$ is invariant and $\mathbf{B}_1$ in global coordinates (denoted $\tilde{\mathbf{B}}_1$) is composed of the directional cosines of the bar element, i.e.

$$\tilde{\mathbf{B}}_1 = \frac{1}{L^{(e)}}\left[-\left(\frac{\mathbf{X}_b - \mathbf{X}_a}{L^{(e)}}\right)^{\mathrm{T}} \quad \left(\frac{\mathbf{X}_b - \mathbf{X}_a}{L^{(e)}}\right)^{\mathrm{T}}\right], \tag{2.18}$$

where $\mathbf{X}_a$ and $\mathbf{X}_b$ are the global coordinates of nodes a and b, respectively.

(c) Rotational spring elements: basic description

For each rotational hinge that represents either a folding crease or bending diagonal on a panel, its degree of rotation (or bending), measured by the dihedral angle between two planar surfaces, is completely defined from the displacements and original coordinates of nodes. In the bar-and-hinge model, a rotational spring element consists of four neighbouring nodes, which forms two triangles, as shown in figure 3.

We denote the undeformed length of a rotational hinge (axis) as $L^{(r)}$. The rotational spring elements are directly defined based on the nodal coordinates, and thus nodal displacements. Therefore, no shape function is required and, as we directly work in the global coordinates, we do not need to perform any transformation from local to global coordinates or vice versa. We assume that the constitutive relationship for each rotational spring element is described by a stored energy

function $\psi = \psi(\theta)$, where θ is the dihedral angle. Thus, the total stored energy in a rotational spring element is

$$U_{\text{spr}}^{(r)} = \psi(\theta). \tag{2.19}$$

We can define the resistance moment as

$$M = \frac{\partial \psi(\theta)}{\partial \theta}. \tag{2.20}$$

The internal force vector associated with a rotational spring element is obtained as

$$\mathbf{T}_{\text{spr}}^{(r)}(\mathbf{u}) = \tilde{\mathbf{T}}_{\text{spr}}^{(r)}(\mathbf{x}) = \frac{\mathrm{d}\psi}{\mathrm{d}\theta}\frac{\mathrm{d}\theta}{\mathrm{d}\mathbf{x}} = M\frac{\mathrm{d}\theta}{\mathrm{d}\mathbf{x}^{(\mathrm{r})}}. \tag{2.21}$$

The nodal coordinates $\mathbf{x}^{(r)}$ determine the value of the associated dihedral angle. Recalling that $\mathbf{u} = \mathbf{x} - \mathbf{X}$, because $\mathbf{X}$ is constant, gradients with respect to $\mathbf{u}$ are equal to gradients with respect to $\mathbf{x}$. The tangent stiffness matrix of a rotational spring element r is then derived as the derivative of the internal force vector:

$$\mathbf{K}_{\text{spr}}^{(r)}(\mathbf{u}) = \tilde{\mathbf{K}}_{\text{spr}}^{(r)}(\mathbf{x}) = k\frac{\mathrm{d}\theta}{\mathrm{d}\mathbf{x}^{(\mathrm{r})}} \otimes \frac{\mathrm{d}\theta}{\mathrm{d}\mathbf{x}^{(\mathrm{r})}} + M\frac{\mathrm{d}^2\theta}{\mathrm{d}(\mathbf{x}^{(\mathrm{r})})^2}. \tag{2.22}$$

The symbol '$\otimes$' means the tensor product. The tangent rotational stiffness k is defined by

$$k = \frac{\mathrm{dM}}{\mathrm{d}\theta}. \tag{2.23}$$

The coupling effect between in-plane behaviour (W) and out-of-plane performance (ψ) of origami sheets is not yet well understood. We avoid adding arbitrary and artificial coupling at the current stage by assuming that ψ is only a function of θ, and θ will not affect the stiffness of bars (W). The above formulation generalizes the linear rotational spring model to a nonlinear model, which allows for additional flexibilities when accounting for specific material properties of the panels.

(d) Geometry of rotational spring element: enhanced description

To complete the formulation of a rotational spring element as defined in §2c, we need to obtain the geometric terms, i.e. the dihedral angle and its derivatives with respect to current configuration (same as to nodal displacements). We remark that the common approach of using direct differentiation of trigonometric functions [14,25] to handle these terms is not sufficient for a robust nonlinear analysis because of the limitations and singularities associated with trigonometric functions. Therefore, in this section, we present the enhanced formulae that will eventually lead to a robust numerical implementation. As shown in figure 4, the geometry of a rotational spring element consists of four nodes (i, j, k, ℓ), two triangles, and one dihedral angle (θ). The two triangles lie on two intersecting planes. Let us denote a vector connecting any two nodes as

$$\boldsymbol{r}_{pq} = \mathbf{x}_p^{(r)} - \mathbf{x}_q^{(r)}, \tag{2.24}$$

where p and q are the labels of any pair of nodes. In addition, we define the normal vectors:

$$\boldsymbol{m} = \boldsymbol{r}_{ij} \times \boldsymbol{r}_{kj} \quad \text{and} \quad \boldsymbol{n} = \boldsymbol{r}_{kj} \times \boldsymbol{r}_{k\ell}, \tag{2.25}$$

where i, j, k, ℓ are labels of the nodes associated with a rotational spring element as marked in figure 4. The two vectors $\boldsymbol{m}$ and $\boldsymbol{n}$ point to the normal directions of the two intersecting planes. The operator '$\times$' between two vectors denotes the cross product. In this paper, repeated indices do not imply summation. Using this notation, the dihedral angle between the two triangles can be determined by

$$\theta = \arccos\left(\frac{\boldsymbol{m}\cdot\boldsymbol{n}}{\|\boldsymbol{m}\|\|\boldsymbol{n}\|}\right). \tag{2.26}$$

However, this expression is not enough to describe the whole range of rotation, because there is no distinction for angles within the ranges of $[0, \pi)$ and $[\pi, 2\pi)$. Therefore, we introduce the

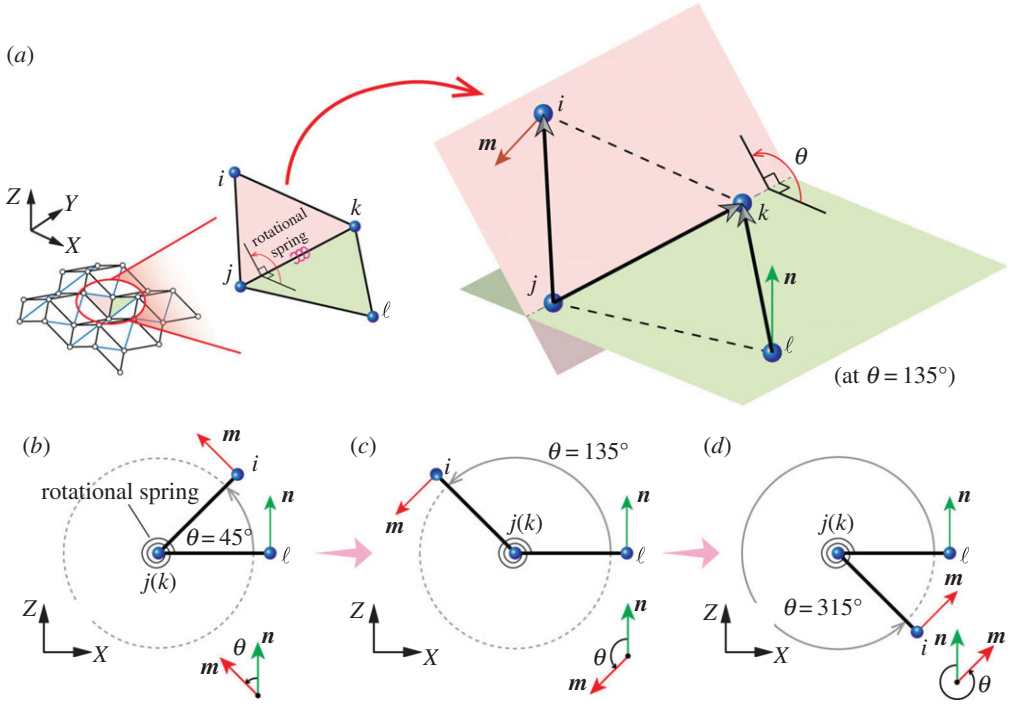

Figure 4. (*a*) Geometry of a rotational spring element. The two triangles lies on two intersecting planes, painted with two different colours. The three space vectors (i.e. $\boldsymbol{r}_{ij}, \boldsymbol{r}_{kj}, \boldsymbol{r}_{k\ell}$), drawn with solid lines are sufficient to define the dihedral angle between the two planes. (*b*)–(*d*) An illustration of the consistent assignment for rotation angle θ of a rotational spring element turning from 0 to 2π (360°). (Online version in colour.)

following definition to expand the domain of definition to $[0, 2\pi)$, that is:

$$\theta = \eta \arccos\left(\frac{\boldsymbol{m}\cdot\boldsymbol{n}}{\|\boldsymbol{m}\|\|\boldsymbol{n}\|}\right) \mod 2\pi, \tag{2.27}$$

where η is a sign indicator defined as,

$$\eta = \begin{cases} \operatorname{sgn}(\boldsymbol{m}\cdot\boldsymbol{r}_{k\ell}), & \boldsymbol{m}\cdot\boldsymbol{r}_{k\ell} \neq 0; \\ 1, & \boldsymbol{m}\cdot\boldsymbol{r}_{k\ell} = 0. \end{cases} \tag{2.28}$$

The symbol 'mod' means modulo operation. The exception of $\boldsymbol{m}\cdot\boldsymbol{r}_{k\ell} = 0$ occurs when the dihedral angle is 0 or π, i.e. the two triangular panels lie on the same plane. Thus adopting equation (2.27), we get a consistent description for all possible rotations of two origami panels if penetration does not happen, that is, from 0 to 2π, as shown in figure 4*b–d*.

Such a large range of rotation (θ varying from 0 to 2π) makes it possible for a mountain fold to become a valley and vice versa. The transition between mountain and valley folds is naturally included in our model. Because our formulation follows an energy approach, it handles both mountain and valley folds in a unified way. For instance, when a mountain fold transitions to a valley fold, it passes through the 'flat state', which corresponds to $\theta = \pi$. Because we define our constitutive model for rotational springs for the range from 0 to 2π, $\theta = \pi$ is a regular state during the rotation process. Thus, we do not need any special treatment to handle switching between mountain and valley folds.

Next, we need the first derivative of the rotation angle with respect to nodal coordinates. Differentiation using the chain rule results in formulae that become numerically unstable

near the angles 0 and π, because of the sine function in the denominator, as shown in equations (2.29)–(2.32):

$$\frac{\partial\theta}{\partial \mathbf{x}_i^{(r)}} = \frac{-1}{\sin(\theta)} \boldsymbol{r}_{kj} \times \frac{\|\boldsymbol{m}\|^2 \boldsymbol{n} - (\boldsymbol{m}\cdot\boldsymbol{n})\boldsymbol{m}}{\|\boldsymbol{m}\|^3 \|\boldsymbol{n}\|}, \tag{2.29}$$

$$\frac{\partial\theta}{\partial \mathbf{x}_\ell^{(r)}} = \frac{-1}{\sin(\theta)} \boldsymbol{r}_{kj} \times \frac{\|\boldsymbol{n}\|^2 \boldsymbol{m} - (\boldsymbol{n}\cdot\boldsymbol{m})\boldsymbol{n}}{\|\boldsymbol{n}\|^3 \|\boldsymbol{m}\|}, \tag{2.30}$$

$$\frac{\partial\theta}{\partial \mathbf{x}_j^{(r)}} = \frac{-1}{\sin(\theta)} \left((\boldsymbol{r}_{ij} - \boldsymbol{r}_{kj}) \times \frac{\|\boldsymbol{m}\|^2 \boldsymbol{n} - (\boldsymbol{m}\cdot\boldsymbol{n})\boldsymbol{m}}{\|\boldsymbol{m}\|^3 \|\boldsymbol{n}\|} - \boldsymbol{r}_{k\ell} \times \frac{\|\boldsymbol{n}\|^2 \boldsymbol{m} - (\boldsymbol{n}\cdot\boldsymbol{m})\boldsymbol{n}}{\|\boldsymbol{n}\|^3 \|\boldsymbol{m}\|} \right) \tag{2.31}$$

and

$$\frac{\partial\theta}{\partial \mathbf{x}_k^{(r)}} = \frac{-1}{\sin(\theta)} \left((\boldsymbol{r}_{k\ell} - \boldsymbol{r}_{kj}) \times \frac{\|\boldsymbol{n}\|^2 \boldsymbol{m} - (\boldsymbol{n}\cdot\boldsymbol{m})\boldsymbol{n}}{\|\boldsymbol{n}\|^3 \|\boldsymbol{m}\|} - \boldsymbol{r}_{ij} \times \frac{\|\boldsymbol{m}\|^2 \boldsymbol{n} - (\boldsymbol{m}\cdot\boldsymbol{n})\boldsymbol{m}}{\|\boldsymbol{m}\|^3 \|\boldsymbol{n}\|} \right). \tag{2.32}$$

These expressions contain terms that will reach singularity when $\sin(\theta) = 0$. Theoretically, these formulae have well-defined limits as $\sin(\theta)$ approaches 0, but in numerical computation, such singularities cannot be handled by floating point arithmetic. The use of inverse sine function to define θ leads to the same problem [25].

Therefore, we move from a trigonometric-based approach to an approach based on distance vectors and functions. By means of some simplifying transformations [42,43], one can obtain equivalent expressions for the gradients that are free of any singularities in their terms, as shown below:

$$\frac{\partial\theta}{\partial \mathbf{x}_i^{(r)}} = \frac{\|\boldsymbol{r}_{kj}\|}{\|\boldsymbol{m}\|^2} \boldsymbol{m}, \tag{2.33}$$

$$\frac{\partial\theta}{\partial \mathbf{x}_\ell^{(r)}} = -\frac{\|\boldsymbol{r}_{kj}\|}{\|\boldsymbol{n}\|^2} \boldsymbol{n}, \tag{2.34}$$

$$\frac{\partial\theta}{\partial \mathbf{x}_j^{(r)}} = \left(\frac{\boldsymbol{r}_{ij}\cdot\boldsymbol{r}_{kj}}{\|\boldsymbol{r}_{kj}\|^2} - 1 \right) \frac{\partial\theta}{\partial \mathbf{x}_i^{(r)}} - \frac{\boldsymbol{r}_{k\ell}\cdot\boldsymbol{r}_{kj}}{\|\boldsymbol{r}_{kj}\|^2} \frac{\partial\theta}{\partial \mathbf{x}_\ell^{(r)}} \tag{2.35}$$

and

$$\frac{\partial\theta}{\partial \mathbf{x}_k^{(r)}} = \left(\frac{\boldsymbol{r}_{k\ell}\cdot\boldsymbol{r}_{kj}}{\|\boldsymbol{r}_{kj}\|^2} - 1 \right) \frac{\partial\theta}{\partial \mathbf{x}_\ell^{(r)}} - \frac{\boldsymbol{r}_{ij}\cdot\boldsymbol{r}_{kj}}{\|\boldsymbol{r}_{kj}\|^2} \frac{\partial\theta}{\partial \mathbf{x}_i^{(r)}}. \tag{2.36}$$

The above equations are actually equivalent to direct differentiations given by equations (2.29)–(2.32), but because they eliminate the sine functions in the denominators, they provide more robust and simpler formulae, which dramatically increase the accuracy and efficiency of numerical evaluations. Details of the simplification are elaborated in appendix A.

These simplified gradients also provide physical insight into the internal forces generated by a rotational spring. For example, from equations (2.33) *and* (2.34)*, we see that the internal force at node i contributed by the rotational spring is always along the direction of* $\boldsymbol{m}$*, and the internal force at node* ℓ *is always along the direction of* $\boldsymbol{n}$*. The math directly reflects the physics: the torque generated by the rotational spring along axis* $\boldsymbol{r}_{kj}$ *results in a perpendicular force on each of the two intersecting panels.*

By differentiating the above formulae, we obtain the second-order derivative (i.e. the Hessian) of the rotation angle with respect to nodal coordinates, which is used to construct the tangent stiffness matrix associated with a rotational spring element (see equation (2.22)). The complete Hessian has 16 blocks of submatrices, where each block is of size 3 by 3, referring to the 3 degrees-of-freedom (x, y, z) at a node. Owing to symmetry of the Hessian, we only need to derive 10 blocks of such submatrices. For example, the first block, i.e. derivative with respect to the 3 degrees-of-freedom at node i, is given by

$$\frac{\partial^2\theta}{\partial(\mathbf{x}_i^{(r)})^2} = -\frac{\|\boldsymbol{r}_{kj}\|}{\|\boldsymbol{m}\|^4} (\boldsymbol{m} \otimes (\boldsymbol{r}_{kj} \times \boldsymbol{m}) + (\boldsymbol{r}_{kj} \times \boldsymbol{m}) \otimes \boldsymbol{m}), \tag{2.37}$$

which is clearly symmetric. The complete expressions for the 16 blocks are elaborated in appendix A. The correctness of the formulae is verified by comparing analytical expressions with finite difference (FD) approximations [44], which is presented in appendix B.

(e) Constitutive relationships for bars

As discussed in §2b, the behaviour of bars can be hyperelastic in our formulation. We use the Ogden constitutive model [40] for the numerical examples in this paper. In this section, we look at the implementation of the Ogden model in the nonlinear bar-and-hinge model. In the Ogden model, the strain energy density W is expressed in terms of the principal stretches as follows:

$$W(\boldsymbol{E}) = \hat{W}(\lambda_1, \lambda_2, \lambda_3) = \sum_{j=1}^{N} \frac{\mu_j}{\alpha_j}(\lambda_1^{\alpha_j} + \lambda_2^{\alpha_j} + \lambda_3^{\alpha_j} - 3), \tag{2.38}$$

where λ_j denotes the principal stretches, and N, μ_j and α_j are the material constants. For one-dimensional bar elements, the material is always under uniaxial tension or compression. Thus, only the principal stretch λ_1 is relevant. Starting from the identity $\lambda_1 = \sqrt{2E_X + 1}$ [41] and applying the chain rule, the 2nd Piola-Kirchhoff stress is given by

$$S_X = \frac{\partial W}{\partial E_X} = \frac{\partial \hat{W}}{\partial \lambda_1}\frac{\mathrm{d}\lambda_1}{\mathrm{d}E_X} = \sum_{j=1}^{N} \mu_j \lambda_1^{\alpha_j - 2}. \tag{2.39}$$

Accordingly, the tangent modulus in equation (2.11) is derived as

$$C = \frac{\partial S_X}{\partial E_X} = \frac{\partial S_X}{\partial \lambda_1}\frac{\mathrm{d}\lambda_1}{\mathrm{d}E_X} = \sum_{j=1}^{N} \mu_j(\alpha_j - 2)\lambda_1^{\alpha_j - 4}. \tag{2.40}$$

As the undeformed configuration ($S_X = 0$) is in a stress-free state, we have the constraint for μ_j as

$$S_X = \sum_{j=1}^{N} \mu_j = 0. \tag{2.41}$$

Then, we obtain the tangent modulus

$$C(\lambda_1 = 1) = C_0 = \sum_{j=1}^{N} \mu_j \alpha_j. \tag{2.42}$$

Taking the special case with $N = 2$, we determine all of the material constants by providing α_1, α_2 and the initial tangent modulus C_0. An advantage of the Ogden model is that it can represent a range of hyperelastic behaviour by fine-tuning a few parameters [40,45]. For example, there are three Ogden material models shown in figure 5. Ogden-1 material with parameters $\alpha_1 = 5$ and $\alpha_2 = 1$ behaves similarly to a linear elastic material under small strain. Ogden-2 material is stiffer in compression than in tension, while Ogden-3 material is stiffer in tension than in compression. We will use constitutive models Ogden-1 and Ogden-2 in the numerical examples.

(f) Constitutive relationships for rotational springs

In the literature, rotational hinges in origami structures are usually supposed to be linear elastic [14,20,22,25]. Therefore, following the notation in §2c, the explicit expression for the moment (M) generated by the linear elastic rotational spring is given as

$$M = L^{(r)}k(\theta - \theta_0), \tag{2.43}$$

where k is the rotational stiffness modulus per unit length along the axis (referring to undeformed configuration). The angle θ_0 is the neutral angle where the rotational spring is at a stress-free state. There are two main limitations of the linear model. First, the linear constitutive relationship allows

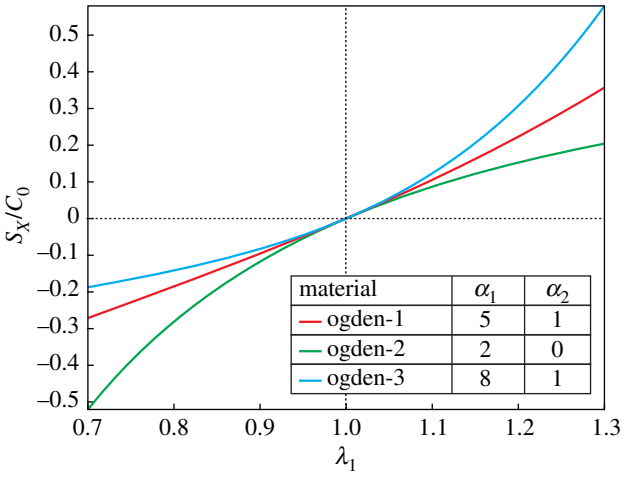

Figure 5. Different hyperelastic material models in uniaxial strain based on the Ogden model. The plot shows normalized (2nd P-K) stress versus principal stretch (λ_1). (Online version in colour.)

for only one adjustable parameter, which is the constant tangent stiffness k. Hence, this model has limited tunability and adaptivity. Second, the linear model does not detect local penetration of origami panels, and thus requires additional kinematic constraints to prevent local penetration. These two drawbacks motivate us to seek new constitutive relations that can provide richer tunability and better physical agreement.

In §2c, we generalized the constitutive relationship for a rotational spring to nonlinear functions. In this section, we introduce a nonlinear constitutive relationship improved from the linear elastic relationship, which assumes that the rotational springs have constant stiffness throughout most of its rotation range, while exhibiting excessive stiffness when the panels are locally close to contact. The expression for M is given as

$$M = \begin{cases} L^{(r)}k_0(\theta_1 - \theta_0) + \left(\dfrac{2k_0\theta_1}{\pi}\right)\tan\left(\dfrac{\pi(\theta-\theta_1)}{2\theta_1}\right), & 0 < \theta < \theta_1; \\ L^{(r)}k_0(\theta - \theta_0), & \theta_1 \le \theta \le \theta_2; \\ L^{(r)}k_0(\theta_2 - \theta_0) + \left(\dfrac{2k_0(2\pi-\theta_2)}{\pi}\right)\tan\left(\dfrac{\pi(\theta-\theta_2)}{4\pi-2\theta_2}\right), & \theta_2 < \theta < 2\pi. \end{cases} \tag{2.44}$$

The constitutive relationship is designed to have a continuous tangent rotational stiffness k for $\theta \in (0, 2\pi)$, as shown below:

$$k = \begin{cases} L^{(r)}k_0 \sec^2\left(\dfrac{\pi(\theta-\theta_1)}{2\theta_1}\right), & 0 < \theta < \theta_1; \\ L^{(r)}k_0, & \theta_1 \le \theta \le \theta_2; \\ L^{(r)}k_0 \sec^2\left(\dfrac{\pi(\theta-\theta_2)}{4\pi-2\theta_2}\right), & \theta_2 < \theta < 2\pi. \end{cases} \tag{2.45}$$

Extremely high stiffness occurs when the dihedral angle approaches 0 or 2π, and thus prevents the local penetration of panels. The physics is clearly indicated by the fact that,

$$\text{as } \theta \to 0 \implies k \to \infty \quad \text{and} \quad \text{as } \theta \to 2\pi \implies k \to \infty. \tag{2.46}$$

The parameters θ_1 and θ_2 can be related to the thickness of the panels. By observation, thicker panels lead to an earlier increase of stiffness when two adjacent panels are close to contact, thus θ_1 and θ_2 should be closer to π (i.e. the flat state). From a practical point of view, θ_1 and

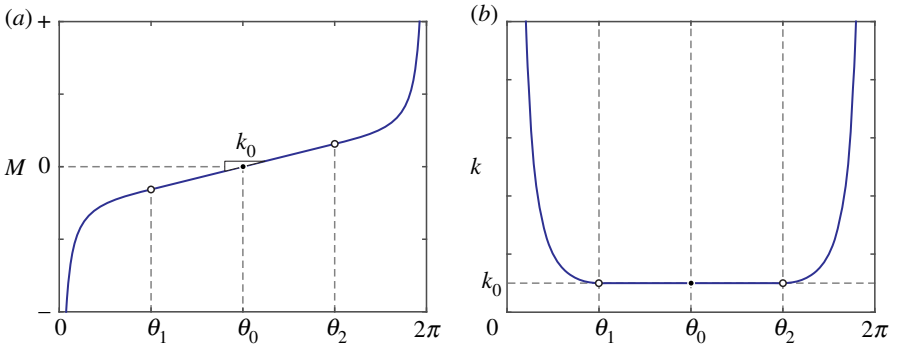

Figure 6. Proposed nonlinear elastic constitutive model of rotational springs, with consideration of local contact. (*a*) dihedral angle versus moment per unit length M, and (*b*) dihedral angle versus tangent rotational stiffness k. The parameters k_0, θ_1 and θ_2 are tunable. The neutral angle θ_0 yields the relaxed state with $M = 0$. (Online version in colour.)

θ_2 shall not be too close to 0 and 2π, respectively, because then a numerical solver may skip sharp increases of stiffness and continue to rotate, allowing penetration. Figure 6 demonstrates the constitutive relationship of rotational springs described by the enriched linear model. In this paper, both the bending and folding of origami structures are treated using the same rotational spring constitutive model with different linear stiffness k_0.

3. A solution scheme for nonlinear analysis

Origami structures are typically subject to highly geometric nonlinearity; however, the conventional Newton–Raphson method is unable to capture the equilibrium path beyond limit points [39,41,46,47]. Thus, to achieve a successful nonlinear analysis of the structure, we need a suitable solution scheme. Here, we use the modified generalized displacement control method (MGDCM) [48], a variant of arc-length methods, as the solver. The MGDCM method has shown its advantages in tracking complicated solution paths of nonlinear problems compared to the standard generalized displacement control method (GDCM) [49]. The method can follow the equilibrium paths with snap-through and snap-back behaviours, and we will verify this using the numerical examples.

The MGDCM solves the equilibrium equation $\mathbf{R}(\mathbf{u}, \lambda) = \mathbf{T}(\mathbf{u}) - \lambda\mathbf{F}$, following an incremental–iterative procedure. The parameter λ is known as the load factor that controls the magnitude of the external loads. The algorithm is summarized in algorithm 1.

In the kth iteration of the ith increment, the load factor increment $\Delta\lambda_k^i$ is determined by Leon *et al*. [48]

$$\Delta\lambda_k^i = \begin{cases} \overline{\Delta\lambda}, & i=1, k=1; \\ -\dfrac{(\Delta\hat{\mathbf{u}}_1^1 \cdot \Delta\check{\mathbf{u}}_k^1)}{(\Delta\hat{\mathbf{u}}_1^1 \cdot \Delta\hat{\mathbf{u}}_k^1)}, & i=1, k>1; \\ \pm\overline{\Delta\lambda}\left|\dfrac{(\Delta\hat{\mathbf{u}}_1^1 \cdot \Delta\hat{\mathbf{u}}_1^1)}{(\Delta\hat{\mathbf{u}}_1^i \cdot \Delta\hat{\mathbf{u}}_1^i)}\right|^{1/2}, & i>1,\ k=1; \\ -\dfrac{(\Delta\hat{\mathbf{u}}_1^i \cdot \Delta\check{\mathbf{u}}_k^i)}{(\Delta\hat{\mathbf{u}}_1^i \cdot \Delta\hat{\mathbf{u}}_k^i)}, & i>1,\ k>1. \end{cases} \tag{3.1}$$

The sign of the load factor increment in the third expression of equation (3.1) is determined by $\operatorname{sgn}(\Delta\hat{\mathbf{u}}_1^{i-1} \cdot \Delta\hat{\mathbf{u}}_1^i)$. The parameter $\overline{\Delta\lambda}$ is the prescribed initial load factor. Typically, the choice of $\overline{\Delta\lambda}$ can play a major role in arc-length methods, and generally small values are good for capturing complex nonlinear behaviours. Sometimes, even a slight change in the initial load factor may lead

Algorithm 1. MGDCM.

$\mathbf{u}_0^1 \leftarrow \mathbf{0}$, $\lambda_0^1 \leftarrow 0$ ▷ Initialization
for $i = 1$ to a specified increment number **do**
  $k \leftarrow 0$
  while $\|\Delta\mathbf{u}_k^i\| > tol$ **do**
    $k \leftarrow k + 1$
    $\mathbf{T}_{k-1}^i \leftarrow \mathbf{T}(\mathbf{u}_{k-1}^i)$, $\mathbf{K}_{k-1}^i \leftarrow \mathbf{K}(\mathbf{u}_{k-1}^i)$
    $\mathbf{R}_{k-1}^i \leftarrow \lambda_{k-1}^i \mathbf{F} - \mathbf{T}_{k-1}^i$
      ▷ Compute internal forces, tangent stiffness matrix and residual vector
    Solve $\mathbf{K}_{k-1}^i \Delta\hat{\mathbf{u}}_k^i = \mathbf{F}$, $\mathbf{K}_{k-1}^i \Delta\check{\mathbf{u}}_k^i = \mathbf{R}_{k-1}^i$
    Determine $\Delta\lambda_k^i$
    $\Delta\mathbf{u}_k^i \leftarrow \Delta\lambda_k^i \Delta\hat{\mathbf{u}}_k^i + \Delta\check{\mathbf{u}}_k^i$ ▷ Notice for $k = 1$, $\Delta\check{\mathbf{u}}_1^i = \mathbf{0}$
    $\mathbf{u}_k^i \leftarrow \mathbf{u}_{k-1}^i + \Delta\mathbf{u}_k^i$, $\lambda_k^i \leftarrow \lambda_{k-1}^i + \Delta\lambda_k^i$ ▷ Compute iterative update
  end while
end for

to poor convergence. However, the MGDCM is not very sensitive to the value of the initial load factor, which means that we can get convergent solutions for a relatively wide range of $\overline{\Delta\lambda}$ [48].

4. Origami simulations

In this section, the nonlinear bar-and-hinge model is applied to structural analyses of various origami structures. The examples start with a simple folding mechanism which is composed of two triangular panels with a single joint line. The numerical results are compared with analytical solutions to verify the implementation of the formulation. It is then followed by analyses of the well-known Miura-ori, under different boundary conditions. The simulations are compared with experiments performed using actual paper-made models. The last example tries to capture the multi-stable behaviour of a helical origami tower structure, known as the Kresling pattern [50] (E.A. Paulino 2015, personal communication). Simulations are conducted using the 'MERLIN' software [38], which is included as electronic supplementary material. Computational time is provided to roughly show the efficiency of the software.[1]

In the examples, the properties of rotational spring elements are defined as described in §2f. The tunable parameters are: (i) initial stiffness modulus: k_0^{F} represents folding of hinges and k_0^{B} represents bending of panels; (ii) the partitions θ_1, θ_2 of the linear and penalty sections, respectively, which are assumed to be the same for both bending and folding in each example. As for the bar elements, they are assumed to have hyperelastic behaviour as described by the second-term Ogden model based on parameters C_0, α_1 and α_2—see §2e.

To improve the accuracy and robustness of the numerical implementation, we sometimes need to normalize the geometric dimensions of the objects. During normalization, it is important to remember that the material properties also need to be properly scaled.

In the current implementation, the shorter diagonal is always chosen to divide a quadrilateral panel. This can be explained from an energy point of view: if we assume that the panel bending stiffness is the same per unit length along both diagonals, then shorter diagonals are easier to bend and thus require lower energy. This presumption is supported by three-dimensional scanning of a deformed Miura sheet [28], which suggests that the bending of a parallelogram panel results in localized curvature along the shorter diagonal. However, if the two diagonals are the same length, then we have to make an arbitrary choice—improved discretization schemes might be able to avoid this ambiguity.

[1]For reference, the MATLAB implementation was executed on a desktop equipped with Intel Xeon CPU (8 cores, 3.0 GHz).

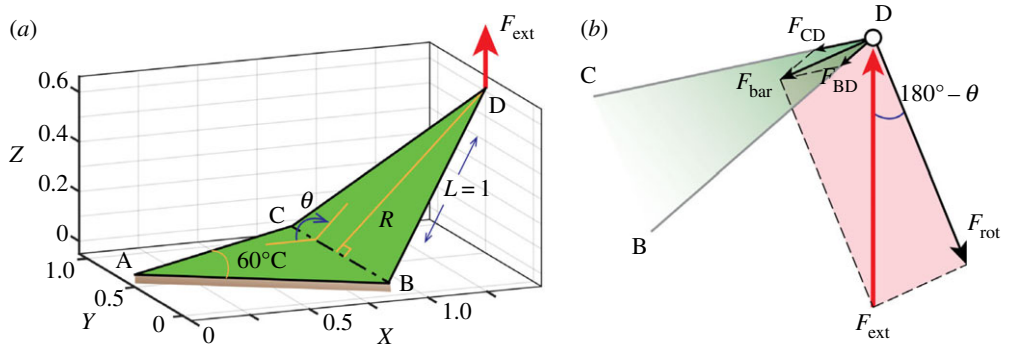

Figure 7. The simple fold example. (*a*) Geometry and boundary conditions. (*b*) Force diagram at node D. (Online version in colour.)

(a) A simple fold

The first example comprises the necessary components for a rotational spring element to exist, namely, four nodes, two triangular panels and one folding crease. The geometry and boundary conditions of the structure are depicted in figure 7*a*. One of the panels is totally fixed on the ground, and the other rotates about the crease line driven by a vertical force applied at the free node D. Based on the bar-and-hinge simplification, the model is composed of one rotational hinge and five bars. To verify the accuracy of the implementation, the numerical solution is compared with analytical derivations.

The initial configuration is assigned with a dihedral angle at $\theta = 135^\circ$, and the rotational spring has a neutral angle at $\theta_0 = 210^\circ$. The values are chosen arbitrarily in order to make a fair evaluation of the accuracy of the numerical implementation. The rotational spring uses the constitutive relationship introduced in §2f, with $\theta_1 = 90^\circ$, $\theta_2 = 210^\circ$ and $k_0 = 1$. The panels are assumed to be rigid, and thus numerically, the bars are assigned a large value for the initial tangent stiffness with $C_0 = 10^{10}$ to asymptotically approach rigidity. The material constitutive relationship for the bar elements follows the pair of parameters: $\alpha_1 = 2$, $\alpha_2 = 0$ (i.e. Neo-Hookean material model, as shown in figure 5), and member areas are assumed to be 10^{-4}. Based on the current setting, the analysis starts from a non-equilibrium state. Guided by the force diagram at node D shown in figure 7*b*, the magnitude of the applied force can be derived as a function of the angle θ,

$$F_{ext} = \frac{F_{rot}}{\cos(\pi - \theta)} = \frac{M(\theta)}{L \sin(\pi/3)\cos(\theta)}. \tag{4.1}$$

The force F_{rot} induced by the rotational spring is always orthogonal to the rotating panel (i.e. the plane of BCD). Note that at the initial configuration, the value of F_{ext} is negative when in equilibrium, meaning that it needs to point upwards. Owing to the symmetry of the structure and boundary conditions, the internal forces in bars BD and CD are of the same magnitude. Therefore, $F_{BD}(=F_{CD})$ can be calculated as

$$F_{BD} = \frac{F_{rot}\tan(\theta)}{2\sin(\pi/3)} = \frac{M(\theta)}{L \sin^2(\pi/3)}. \tag{4.2}$$

The comparisons shown in figure 8 present great agreement between the numerical and analytical solutions. This verification example serves as a reference for other simulations.

(b) Folding and bending of Miura-ori

Miura-ori is one of the most famous patterns in origami engineering and has been studied extensively [5,9,28,51]. This example, as a verification of the proposed nonlinear formulation, compares existing theoretical analyses of Miura-ori [26,29] with our numerical simulations. A

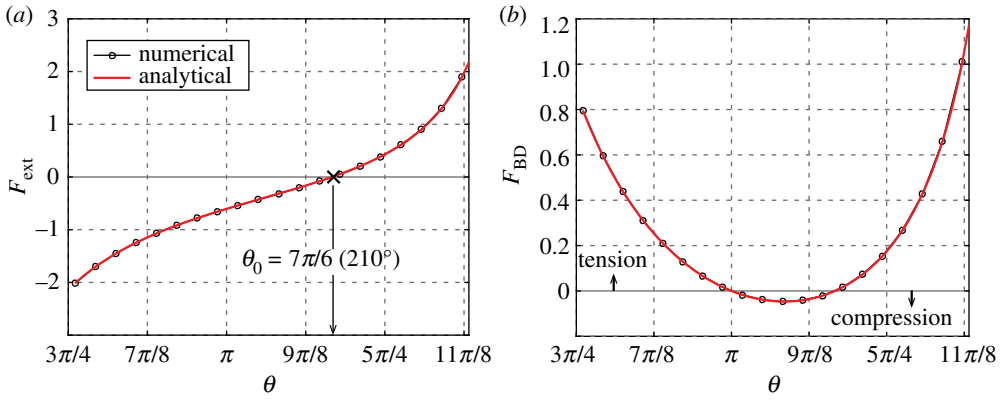

Figure 8. (*a*) Equilibrium path, F_{ext} versus θ. (*b*) F_{BD} versus θ. (Online version in colour.)

Miura-ori can be configured by a few geometric parameters: a, b and α, as shown in figure 9. In this example, we assign the following values: $a = 0.02$, $b = 0.02$ and $\alpha = 60^\circ$. The material properties are determined by the following parameters: folding stiffness $k_0^F = 0.1$, bar element area $A = 1 \times 10^{-5}$ and Ogden model parameters $\alpha_1 = 5$, $\alpha_2 = 1$, i.e. material Ogden-1 as shown in figure 5. Because the theoretical predictions [26,29] are derived without considering surface contact, we do not apply a local collision penalty in this example, so we set $\theta_1 = 0^\circ$, $\theta_2 = 360^\circ$. In the compressed folding test, we adopt a bending stiffness $k_0^B = 10^4$ and stretching stiffness $C_0 = 10^{10}$. For the bending test, i.e. non-rigid Miura-ori case, we reduce the bending stiffness and stretching stiffness to $k_0^B = 1$ and $C_0 = 10^8$, respectively.

The ratio k_0^B/k_0^F is a key parameter that determines whether an origami is close to a mechanism (rigid origami) or not. For example, as $k_0^B/k_0^F \to \infty$, we approach a situation where rigid panels are connected by compliant hinges (rigid origami). When $k_0^B/k_0^F \to 1$, the panel and the fold have the same stiffness (e.g. origami sheet folded from a single material such as metal) [25]. In this example, we use two values for k_0^B/k_0^F. In the folding simulation, we choose a relatively large ratio ($k_0^B/k_0^F = 10^5$), such that the origami structure is asymptotically rigid. In the bending simulation, a smaller ratio ($k_0^B/k_0^F = 10$) is used to simulate a non-rigid origami in which panel bending cannot be neglected.

(i) Rigid Miura-ori: folding

First, we look at the folding kinematics of Miura-ori. The in-plane stiffness and the tangential Poisson's ratio [26,29,52] of Miura-ori have been derived analytically based on the rigid origami assumption, with linear elastic rotational stiffness for the folding hinges [26,29]. If our proposed formulation is correct, then it should be able to asymptotically simulate rigid origami by assigning large panel bending stiffness and stretching stiffness, i.e. k^B and C_0. Applying in-plane compression forces the Miura-ori to fold. We restrict the displacements of nodes at the left end ($x = 0$) to the yz-plane, and fix the node at $(x, y, z) = (0, 0, 0)$ in all three directions. The ground nodes ($z = 0$) to the right end are not allowed to translate in the z-direction. Then, we apply uniform forces of unit magnitude to all the nodes at the right end, towards the left (i.e. $-x$ direction). Figure 9*d* shows a side view of the boundary condition.

The in-plane compression starts from an almost flat state. We compare the load-displacement curve and tangential Poisson's ratio curve, obtained by the numerical method, with the analytical predictions in [29]. The tangential Poisson's ratio describes the Poisson's ratio of a material at an infinitesimal deformation limit, deviating from the current deformed configuration [26,29]. The ratio is defined as follows:

$$\nu_{LW} = -\frac{\mathrm{d}W/W}{\mathrm{d}L/L} = -\frac{L}{W}\frac{\mathrm{d}W}{\mathrm{d}L}, \tag{4.3}$$

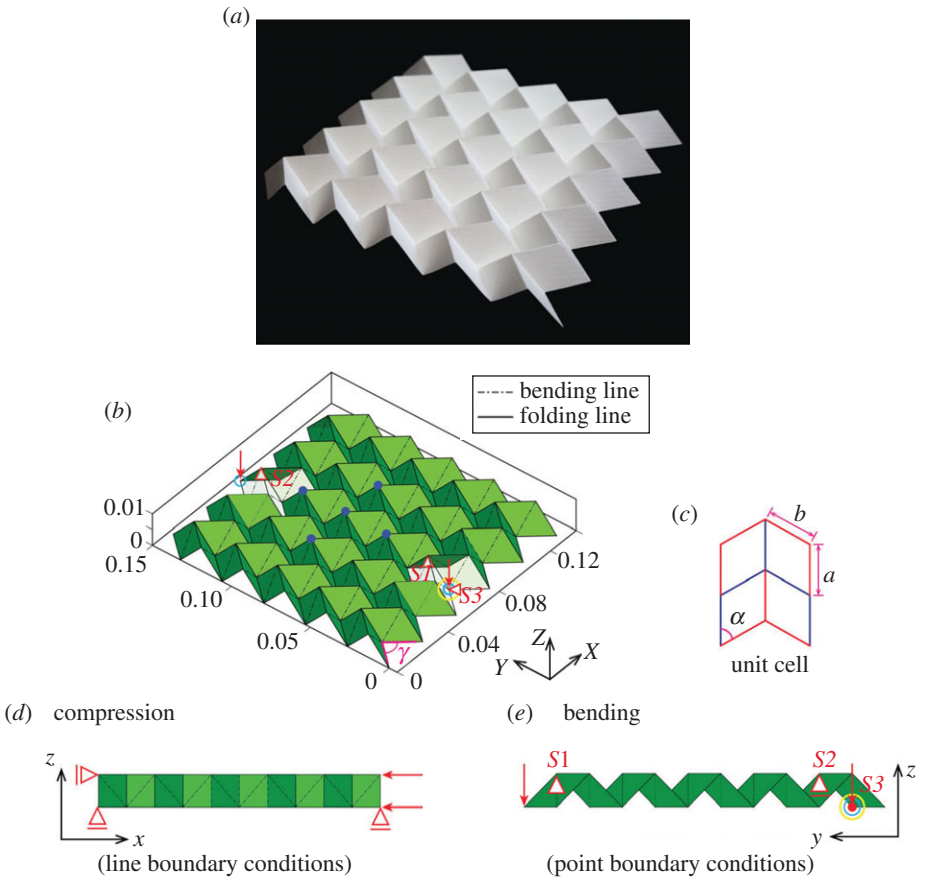

Figure 9. (*a*) Paper-made Miura-ori model. (*b*) An isometric view of the initial configuration of the numerical model and boundary conditions for the bending simulation. The angle γ between two edges is used to specify the initial configuration of a Miura-ori, which equals 118.27° for the compression simulation and 90° for the bending simulation. In the bending simulation, support *S1* restricts displacements in *x*-, *y*-, *z*-directions; *S2* fixes *x*-, *z*-directions; *S3* confines only *x* translations. Unit forces are applied towards the $-z$ direction on nodes marked with blue circles. Displacement Δ is measured at one of the loading nodes as the *z*-displacement, marked with a yellow circle (same node as *S3*). The blue dots show the nodes that are used to approximate the global principal curvatures near the centre of the origami sheet. (*c*) A flattened unit cell of the Miura-ori. We take $a = 0.02$, $b = 0.02$ and $\alpha = 60°$ for the simulations. (*d*) Illustration of the boundary conditions in the compression simulation from a side view. (*e*) Side view of the boundary conditions for the bending simulation. (Online version in colour.)

where W and L are the bulk dimensions of a Miura-ori as depicted in figure 10*b*. Other measures of the effect might be used to consider the large deformation nature of origami, such as the Poisson function [53,54]. Here, we adopt the same tangential Poisson's ratio definition as used for the theoretical predictions to show that our proposed formulation is able to asymptotically capture the correct kinematics of rigid origami. The theoretical Poisson's ratio for a Miura-ori is given as [26,29]

$$\nu_{LW} = -\tan^2\left(\frac{\gamma}{2}\right), \tag{4.4}$$

where angle γ is illustrated in figure 9*b* (close to the origin). We plot the tangential Poisson's ratio with respect to the folding ratio (i.e. L/L_{unfold} as shown in figure 10) of the Miura-ori, which equals 1 when the origami is fully flat, and 0 when fully folded. To get the numerical approximation, we first interpolate the discrete values of W and L at all load steps to a continuous function using

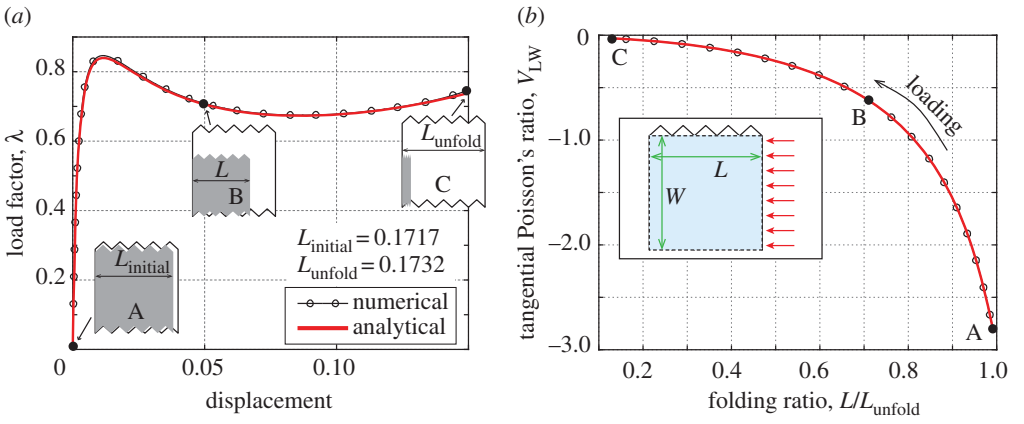

Figure 10. Compressed folding of Miura-ori. The in-plane compression starts from an almost flat state (i.e. at L_{initial}). (*a*) Equilibrium path, displacement versus load factor (λ). The insets demonstrate the folded shapes along the compression process. The black profiles in the three insets outline the unfolded planar pattern. (*b*) In-plane tangential Poisson's ratio ν_{LW} versus the folding ratio (L/L_{unfold}). The analytical solutions are obtained based on the formulae presented in [29]. (Online version in colour.)

cubic splines, and then compute the Poisson's ratio using equation (4.3). A very good agreement is observed as shown in figure 10.

(ii) Non-rigid Miura-ori: bending

When the Miura-ori has non-rigid panels, it can present global out-of-plane deformations, bending anticlastically into a saddle-shaped configuration. An elegant theoretical derivation by Wei *et al.* [29] shows that the Poisson's ratios of Miura-ori for in-plane and out-of-plane infinitesimal deformation have equal magnitude, but opposite signs. The analytic bending Poisson's ratio is derived assuming that there are periodic small deformations of unit cells. For a large global bending deformation, the unit cells of Miura-ori actually deform non-uniformly throughout the sheet [26,29]. Therefore, the applicable range of this analytical expression for the bending Poisson's ratio is limited. The proposed numerical approach provides a way to numerically predict the global bending behaviour of Miura-ori under large deformation. Because the bending Poisson's ratio is not well-defined for the large deformation case, we instead compute the coupling ratio of the two principal curvatures of the sheet, i.e. $-\kappa_x/\kappa_y$, as shown in figure 11. For small deformations, this coupling ratio equals the bending Poisson's ratio as defined in [29]. We adopt the values of input parameters for the compression test, except reduced bending stiffness and stretching stiffness ($k_0^{\text{B}} = 1$ and $C_0 = 10^8$), in order to represent non-rigid panels. Boundary conditions are shown in figure 9*b*,*e*.

In the bending simulation, the Miura-ori is initially partially folded. The computation takes about 7 s with $\overline{\Delta\lambda} = 0.03$. The analysis successfully predicts the saddle-shaped deformation of the Miura-ori. The load-displacement curve is shown in figure 11*a*. The coupling ratio ($-\kappa_x/\kappa_y$) is interpolated near the centre of the sheet using five nodes on the upper surface as marked with blue dots in figure 9*b*. When the deformation is small (at point A), the ratio is close to 1.0, agreeing with the analytical prediction. As the deformation gets larger, the unit cells deform heterogeneously and the coupling ratio increases. The obtained deformation shows a qualitatively good agreement with that of the paper-made model, as demonstrated in figure 11*b*,*c*.

(c) Pop-through defect of Miura-ori: bistability

Miura sheets may display a local bistable behaviour. Silverberg *et al.* [28] named such behaviour as 'pop-through defects', and studied their influence on the mechanical properties of Miura-ori

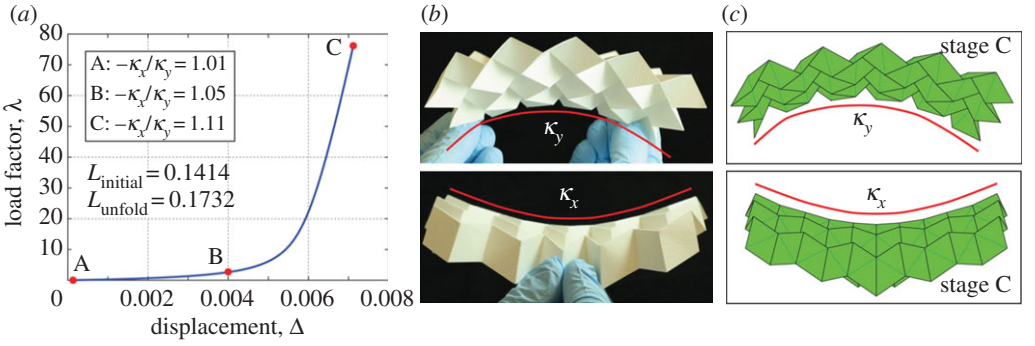

Figure 11. Bending of Miura-ori. (*a*) Equilibrium path, displacement Δ versus load factor λ. Displacement Δ is measured at one of the loading nodes as the *z*-displacement, as shown in figure 9. (*b*) Two views of the final state (at point C) of the bended Miura-ori, with pictures of both the paper model and the numerical model. (Online version in colour.)

structures. Figure 12*a* shows a regular configuration of Miura-ori, while on the side, figure 12*b* shows a Miura-ori with a central unit cell in the 'pop-through' state. The 'pop-through' state can be achieved by applying a vertical force to a vertex until the unit cell pops into another mechanically stable state. The soft bending of panels is the main contributor to this phenomenon [28].

The deformation process that forms a 'pop-through' state has not been investigated yet, and thus it is the subject of this study. We consider a Miura-ori structure with the same geometry as the previous example presented in §4b. The Ogden-1 material model is used for bar elements. Other material related parameters are: $k_0^{\mathrm{F}} = 0.1$, $k_0^{\mathrm{B}} = 1$, $C_0 = 1 \times 10^8$, $A = 1 \times 10^{-5}$. We consider contact of adjacent panels by setting $\theta_1 = 45^\circ$, $\theta_2 = 315^\circ$. The initial state and boundary conditions are shown in figure 12*c*. The initial load factor is $\overline{\Delta\lambda} = 0.06$ and the computational time is approximately 11 s. Figure 13 shows the equilibrium path and different deformations under various magnitudes of loading. The corresponding configuration at point C is the stable 'pop-through' state when the structure is in self-equilibrium. The numerical simulation approximately reproduces the formation of the 'pop-through defect' of the paper-made model. Under the given load, the Miura-ori presents a typical curve of bistability with snap-through behaviour [39,46], as indicated in figure 13.

(d) Multi-stability of the Kresling pattern

The Kresling pattern [50] is a type of cylindrical shell origami that has multi-stable behaviour [55]. The nodes of the Kresling pattern lie on the intersection of two sets of helices (longitudinal) and one set of circles (transverse). A commercial company has used the idea of Kresling pattern to fabricate foldable wine bags as shown in figure 14*a*, which forms stable structures in both a folded and deployed state (E.A. Paulino 2015, personal communication). In this example, we look at the equilibrium path of such multi-stable behaviour using the proposed nonlinear bar-and-hinge model.

According to Cai *et al.* [55], the multi-stability of this structure is due to the change of crease lengths. In other words, the multi-stable behaviour originates from panel stretching, instead of panel bending as in the previous example. The numerical model has three layers, each modelling one section of the origami wine bag. We assign $k_0^{\mathrm{F}} = 1 \times 10^{-3}$, $\theta_1 = 45^\circ$, $\theta_2 = 315^\circ$ and $C_0 = 5 \times 10^7$ as the basic material properties. The Ogden-1 material model is used for bar elements. The folding stiffness is very small because we observe that the folding creases of the physical model (i.e. the origami wine bag as shown in figure 14*a*) are quite soft. The cross-sectional areas of the bar elements are 10^{-5}. This pattern has only triangular panels and they are not further discretized in the bar-and-hinge model. Therefore, there are no bending hinges. The boundary conditions

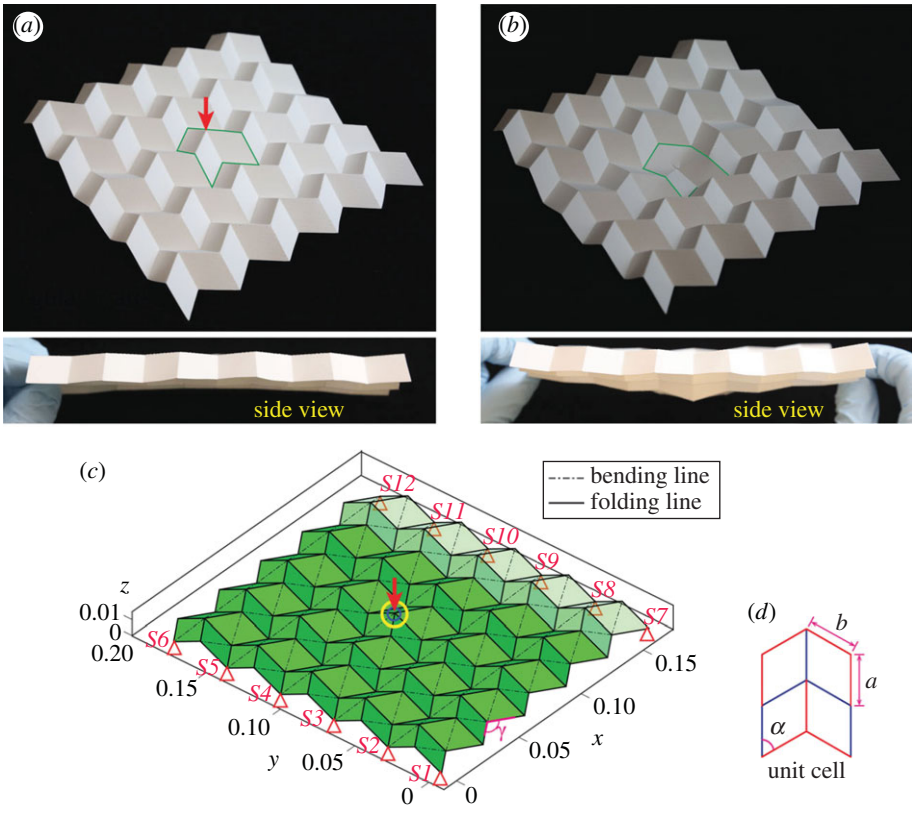

Figure 12. The Miura-ori 'pop-through defect'. (*a*) The paper-made Miura-ori model in a regular partially folded configuration. (*b*) The Miura-ori model in the 'pop-through' state, which is a stable configuration. (*c*) The numerical model and boundary conditions for simulation. The angle γ is 112.61°. Support *S1* fixes displacements in *x*-, *y*-, *z*-directions, *S2*–*S6* fix displacements in *x*-, *z*-directions and *S7* fixes *y*-, *z*-displacements. From *S8* to *S12*, restrictions only apply in the *z*-direction. Load is applied as a unit force towards the $-z$ direction on the node marked with blue circle. Displacement Δ is the *z*-displacement measured at the loading node — also marked with a yellow circle. (*d*) A flattened unit cell of the Miura-ori. We take $a = 0.02$, $b = 0.02$ and $\alpha = 60°$. (Online version in colour.)

for the simulations are shown in figure 14*b*. The bottom of the tower is fixed on the ground in all directions.

The investigation is conducted by applying uniform unit compression forces on the top nodes. An initial load factor $\overline{\Delta\lambda} = 0.032$ is used. The execution time of the analysis is 4 s. The equilibrium path shown in figure 14*c* draws the downward displacement of a top node versus the value of the load factor. This diagram can be seen as a projection of the multi-dimensional equilibrium path onto the specific plane of Δ and λ. It is interesting that the equilibrium path makes a U-turn at point C, and then traces a path of almost identical projection as the previously passed. In actuality, however, the two almost overlapping paths refer to completely different deformations, as illustrated in figure 14*c* with the insets and figure 14*e*–*g*. For example, coincident points B and D, on the first and second passes, respectively, refer to different stable states of the origami structure, as shown in figure 14*f*,*g*. At point B, the middle layer is fully folded, while at point D, the middle layer reopens. From the stored energy diagram, we can clearly see that B and D are two different local minima. The distribution of stored energy verifies that, for such an origami structure, the non-rigid behaviour comes mostly from the stretching deformation of the panels.

We note here that such multi-stable structures typically have many bifurcation points and branches on the equilibrium paths; however, the solution solver (MGDCM) would only pick one

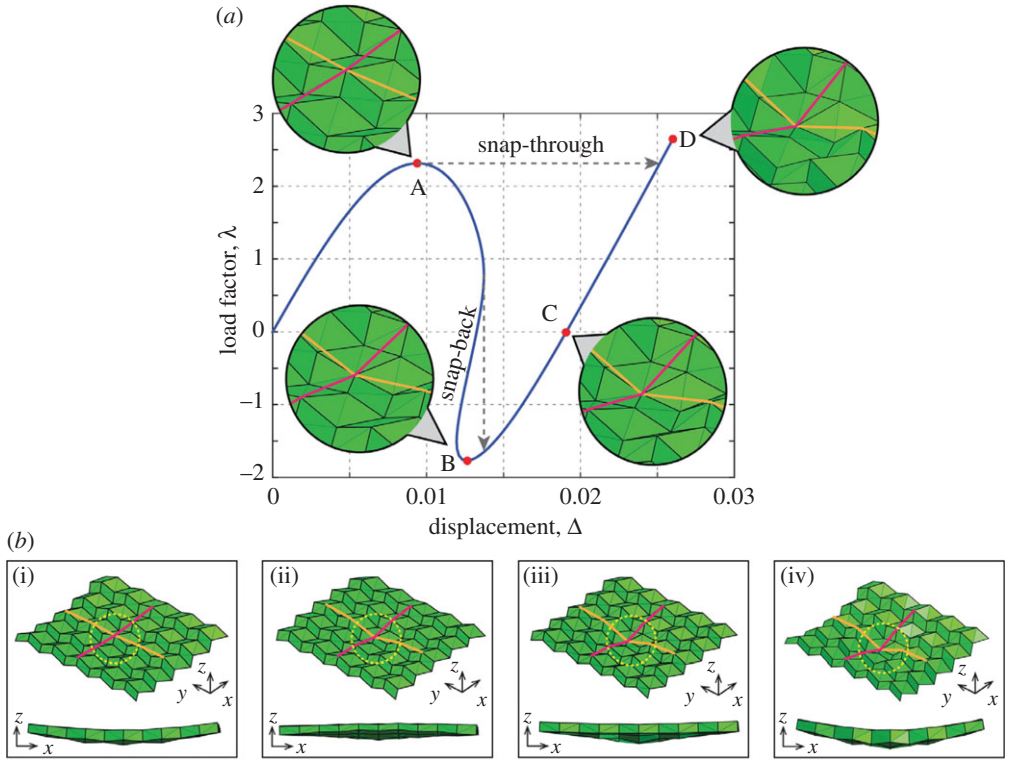

Figure 13. (*a*) Equilibrium path, Δ versus λ, during the deformation process of a 'pop-through defect' on Miura-ori. The insets show zoom-in views of the deformed Miura-ori near the central region. Reference of these insets to the global configuration is illustrated in (*b*). (*b*) Several key frames of deformed configurations along the simulation, corresponding to the four points (A–D) on the equilibrium path. At stage C, the corresponding configuration is in a stable state, and the digital rendering shows a similar configuration to the physical model shown in figure 12(*b*). The yellow dashed circles mark the zoom-in regions for insets in (*a*). (Online version in colour.)

of the many branches. The choice of branch that the solver selects depends on many factors, including the value of the initial load factor $\overline{\Delta\lambda}$. In general, the choice of branching appears to be arbitrary. Despite this insufficiency of the nonlinear solver, this example indicates that our nonlinear formulation is able to present the full picture of the deformation spaces of multi-stable origami structures, because we (at least) captured two equilibrium states other than the initial configuration in this example. Numerical techniques for bifurcation analysis [41] may allow us to guide the nonlinear solver to follow a specific branch of the equilibrium paths, which is a possible improvement of the current nonlinear bar-and-hinge model.

Guest & Pellegrino [31,56,57] investigated (numerically and experimentally) a multi-stable triangulated cylinder, which has a similar geometry as the Kresling pattern, but whose nodes are at the intersections of three helices; thus, the transverse edges form helices instead of separate circles as in the Kresling pattern. In their numerical analysis, they simplified the structure into a reduced model, following similar simplifications, as in our study. They conducted a displacement-controlled simulation based on a force method, and found that the contribution of folding hinges to the global mechanical behaviour is small, which agrees with our observation for the Kresling pattern. By contrast, our fully nonlinear formulation uses a highly nonlinear constitutive model of rotational springs to prevent the local intersection of panels, while they handled this issue by adding extra constraints to the system of equations. These extra constraints eliminate the possibility of spring-back of the folded region, which is likely to occur in practice, and is captured in our simulations.

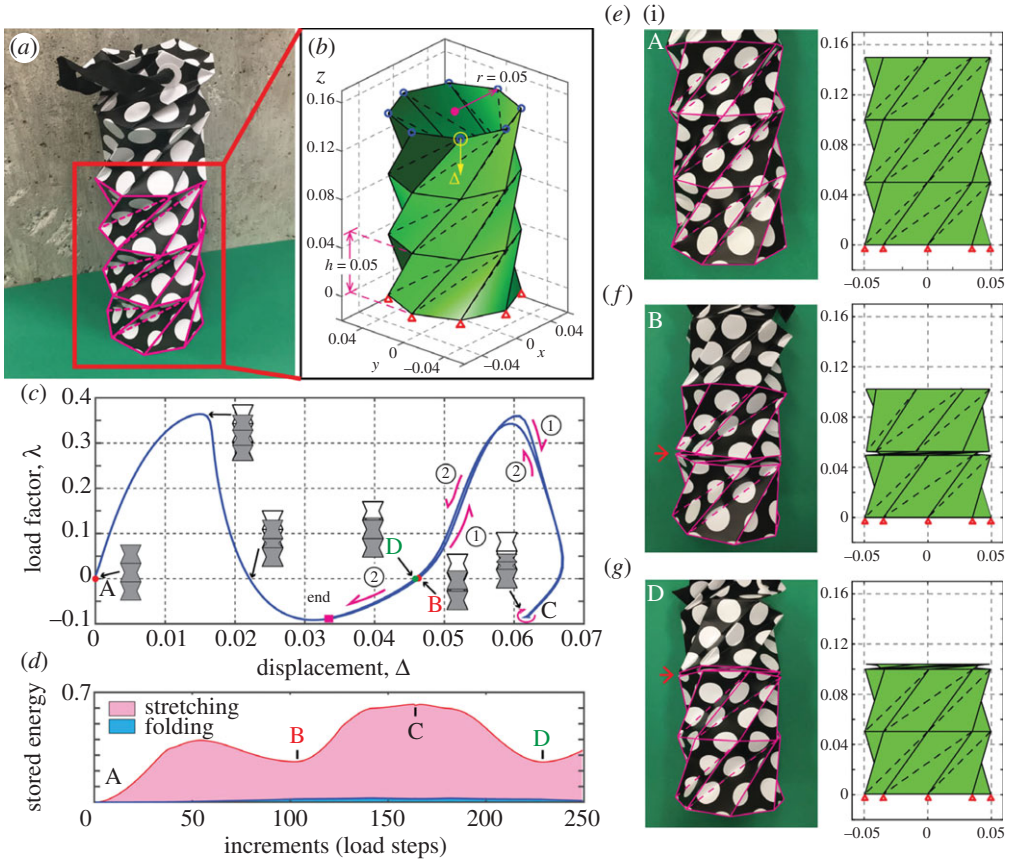

Figure 14. The multi-stable Kresling origami tower. (*a*) An origami wine bag that has the shape of the Kresling pattern with eight sides. (*b*) Geometry and boundary conditions of the numerical model. Each layer of the tower has a height of $h = 0.05$. On each layer, the cross-sectional outline, which is a regular octagon, is placed inside a circle of radius $r = 0.05$. Supports are indicated by red triangles, all of which restrict displacement in the *x*-, *y*-, *z*-directions. Unit forces are applied at nodes circled in blue to the $-z$ direction. Displacement Δ is measured as the *z*-displacement of the node marked with a yellow circle. (*c*) Equilibrium path, Δ versus λ. The insets illustrate the global deformation of the origami at different points on the equilibrium path. At point C, we can see that the top and middle layer have an equal chance to collapse, thus C refers to a bifurcation point. (*d*) Stored energy profile along the simulation process. States A, B and D refer to three local minima on the profile. Energy contributions from stretching deformation and folding deformation are distinguished by different colours. There is no bending deformation considered in this simulation. (*e*, *g*) Stable configurations along the path (at points A, B and D) are demonstrated using side views. We present both key frames from the numerical simulation and corresponding physical model configurations. (Online version in colour.)

5. Conclusion

This paper presents a nonlinear formulation for simulating large displacements and deformations of origami structures, based on the bar-and-hinge model, which is a reduced degree-of-freedom model of origami as pin-jointed bar networks with virtual rotational springs. We hence achieve a computationally efficient approach for understanding the nonlinear mechanics of origami structures when panel deformations are taken into account. Numerical simulations show that the formulation is able to capture key features of origami deformations on a global scale, such as folding kinematics, bending curvatures and multi-stability. Its simplicity and efficiency allows quick investigations of non-rigid origami structures when the global deformation is of primary interest.

When comparing both bar-and-hinge and shell element-based FE models, we note that their simplifications are made at different levels: the bar-and-hinge model is a conceptual simplification of the structural model, while the FE attempts to model the actual structural system while introducing most simplifications at the formulation level. In this context, the bar-and-hinge model is inherently discrete, while the shell element-based FE approaches are continuum-based (cf. [16–19]). As a result, the discrete bar-and-hinge model provides a simpler representation of the actual origami structure than continuous shell elements. For example, it can provide a simpler origami model than those of FE shell models for a system of several components (e.g. facets, joints) made with different materials. In essence, our present bar-and-hinge model provides insight into the nonlinear behaviour of origami structures, and allows highly efficient and effective simulations. It approximates the global behaviour of origami structures, but cannot provide high-resolution minutia of local origami deformations.

The generality of the nonlinear bar-and-hinge structural analysis formulation offers space for further improvement. The constitutive relationships of the bars and rotational springs can be designed to better reflect the physical behaviours of specific origami structures. In addition, because the formulation is compatible with arbitrary bar-and-hinge models, the discretization scheme can be improved. Currently, the adopted discretization scheme is only applicable to origami sheets with triangular and quadrilateral panels. Refined triangulation schemes may be used to improve accuracy and to enable the analysis of origami structures with arbitrary polygonal panels. Furthermore, global contact of the sheets may also be considered.

Ethics. This work did not involve any active collection of human or animal data.

Data accessibility. This work does not have any experimental data.

Authors' contributions. G.H.P. designed the research. G.H.P. and K.L. conceived the mathematical models, interpreted computational results, analysed data and wrote the paper. K.L. implemented the formulation and performed most of the simulations. All the authors gave their final approval for publication.

Competing interests. We have no competing interests.

Funding. This work was supported by the USA National Science Foundation grant no. 1538830, the China Scholarship Council (CSC) and the Raymond Allen Jones Chair at the Georgia Institute of Technology.

Acknowledgements. This paper is dedicated to the memory of Prof. Richard H. Gallagher (1927–1997). The authors extend their appreciation to Mrs Ebertilene A. Paulino for suggesting the investigation of the Kresling pattern. We also thank Mr Zonglin Li for taking photos of the physical origami models.

Disclaimer. The information provided in this paper is the sole opinion of the authors and does not necessarily reflect the views of the sponsoring agencies.

Appendix A. Geometric terms of rotational spring elements

To accomplish the simplification from equations (2.29)–(2.32) to equations (2.33)–(2.36), the following vector identity will be used frequently:

$$\boldsymbol{a} \times (\boldsymbol{b} \times \boldsymbol{c}) = (\boldsymbol{a} \cdot \boldsymbol{c})\boldsymbol{b} - (\boldsymbol{a} \cdot \boldsymbol{b})\boldsymbol{c}. \tag{A 1}$$

Following the procedure as described in [43], let us first simplify equation (2.29) as follows:

$$\begin{aligned}
\frac{\partial \theta}{\partial \mathbf{x}_i^{(r)}} &= \frac{-1}{\sin(\theta)} \boldsymbol{r}_{kj} \times \frac{\|\boldsymbol{m}\|^2 \boldsymbol{n} - (\boldsymbol{m} \cdot \boldsymbol{n})\boldsymbol{m}}{\|\boldsymbol{m}\|^3 \|\boldsymbol{n}\|}, \\
&= \frac{-1}{\sin(\theta)} \boldsymbol{r}_{kj} \times \left(\frac{\boldsymbol{m} \times (\boldsymbol{n} \times \boldsymbol{m})}{\|\boldsymbol{m}\|^3 \|\boldsymbol{n}\|} \right), \\
&= \frac{-1}{\sin(\theta)} \boldsymbol{r}_{kj} \times \left(\frac{\boldsymbol{m} \times (-\sin(\theta)\|\boldsymbol{m}\| \|\boldsymbol{n}\| \boldsymbol{r}_{kj})}{\|\boldsymbol{r}_{kj}\| \|\boldsymbol{m}\|^3 \|\boldsymbol{n}\|} \right), \\
&= \frac{\boldsymbol{r}_{kj} \times \boldsymbol{m} \times \boldsymbol{r}_{kj}}{\|\boldsymbol{r}_{kj}\| \|\boldsymbol{m}\|^2}, \\
&= \frac{\|\boldsymbol{r}_{kj}\|}{\|\boldsymbol{m}\|^2} \boldsymbol{m}.
\end{aligned} \tag{A 2}$$

Because equation (2.30) has the same structure as (2.29), following the same procedure, equation (2.30) can be simplified to equation (2.34). Starting with equation (2.31) and using equation (2.29), we can obtain equation (2.35) by the following transformations:

$$\begin{aligned}\frac{\partial\theta}{\partial\mathbf{x}_j^{(r)}} &= \frac{-1}{\sin(\theta)}\left((\boldsymbol{r}_{ij}-\boldsymbol{r}_{kj})\times\frac{\|\boldsymbol{m}\|^2\boldsymbol{n}-(\boldsymbol{m}\cdot\boldsymbol{n})\boldsymbol{m}}{\|\boldsymbol{m}\|^3\|\boldsymbol{n}\|}-\boldsymbol{r}_{k\ell}\times\frac{\|\boldsymbol{n}\|^2\boldsymbol{m}-(\boldsymbol{n}\cdot\boldsymbol{m})\boldsymbol{n}}{\|\boldsymbol{n}\|^3\|\boldsymbol{m}\|}\right),\\ &= \frac{-1}{\sin(\theta)}\left(\boldsymbol{r}_{ij}\times\frac{\boldsymbol{m}\times(\boldsymbol{n}\times\boldsymbol{m})}{\|\boldsymbol{m}\|^3\|\boldsymbol{n}\|}-\boldsymbol{r}_{k\ell}\times\frac{\boldsymbol{n}\times(\boldsymbol{m}\times\boldsymbol{n})}{\|\boldsymbol{n}\|^3\|\boldsymbol{m}\|}\right)-\frac{\partial\theta}{\partial\mathbf{x}_i^{(r)}},\\ &= -\frac{\boldsymbol{r}_{ij}\times\boldsymbol{m}\times(-\boldsymbol{r}_{kj})}{\|\boldsymbol{r}_{kj}\|\|\boldsymbol{m}\|^2}+\frac{\boldsymbol{r}_{k\ell}\times\boldsymbol{n}\times\boldsymbol{r}_{kj}}{\|\boldsymbol{r}_{kj}\|\|\boldsymbol{n}\|^2}-\frac{\partial\theta}{\partial\mathbf{x}_i^{(r)}},\\ &= \frac{(\boldsymbol{r}_{ij}\cdot\boldsymbol{r}_{kj})\boldsymbol{m}}{\|\boldsymbol{r}_{kj}\|\|\boldsymbol{m}\|^2}+\frac{(\boldsymbol{r}_{k\ell}\cdot\boldsymbol{r}_{kj})\boldsymbol{n}}{\|\boldsymbol{r}_{kj}\|\|\boldsymbol{n}\|^2}-\frac{\partial\theta}{\partial\mathbf{x}_i^{(r)}},\\ &= \left(\frac{\boldsymbol{r}_{ij}\cdot\boldsymbol{r}_{kj}}{\|\boldsymbol{r}_{kj}\|^2}-1\right)\frac{\partial\theta}{\partial\mathbf{x}_i^{(r)}}-\frac{\boldsymbol{r}_{k\ell}\cdot\boldsymbol{r}_{kj}}{\|\boldsymbol{r}_{kj}\|^2}\frac{\partial\theta}{\partial\mathbf{x}_\ell^{(r)}}.\end{aligned}\tag{A 3}$$

Similarly, equation (2.32) has the same structure as (2.31), thus equation (2.36) can be simplified from equation (2.32).

Next, we will elaborate on the Hessian of rotation angles. The Hessian matrix appears in the stiffness matrices of rotational spring elements. The Hessian contains 16 blocks of submatrices (of size 3×3), among which there are 10 independent blocks due to symmetry. For clarity, let us define

$$A=\frac{\boldsymbol{r}_{ij}\cdot\boldsymbol{r}_{kj}}{\|\boldsymbol{r}_{kj}\|^2}\quad\text{and}\qquad B=\frac{\boldsymbol{r}_{k\ell}\cdot\boldsymbol{r}_{kj}}{\|\boldsymbol{r}_{kj}\|^2}.\tag{A 4}$$

Therefore, we obtain the following relationships:

$$\frac{\partial A}{\partial\mathbf{x}_j^{(r)}}=\frac{1}{\|\boldsymbol{r}_{kj}\|^2}((2A-1)\boldsymbol{r}_{kj}-\boldsymbol{r}_{ij}),\tag{A 5}$$

$$\frac{\partial B}{\partial\mathbf{x}_j^{(r)}}=\frac{1}{\|\boldsymbol{r}_{kj}\|^2}(2B\boldsymbol{r}_{kj}-\boldsymbol{r}_{k\ell}),\tag{A 6}$$

$$\frac{\partial A}{\partial\mathbf{x}_k^{(r)}}=\frac{1}{\|\boldsymbol{r}_{kj}\|^2}(-2A\boldsymbol{r}_{kj}+\boldsymbol{r}_{ij})\tag{A 7}$$

and

$$\frac{\partial B}{\partial\mathbf{x}_k^{(r)}}=\frac{1}{\|\boldsymbol{r}_{kj}\|^2}((1-2B)\boldsymbol{r}_{kj}+\boldsymbol{r}_{k\ell}).\tag{A 8}$$

In addition, let us define the operator '$\diamond$' as

$$\boldsymbol{a}\diamond\boldsymbol{b}:=\boldsymbol{a}\otimes\boldsymbol{b}+\boldsymbol{b}\otimes\boldsymbol{a},\quad\forall\boldsymbol{a},\boldsymbol{b}\in\mathbb{R}^3.\tag{A 9}$$

Note that $\boldsymbol{a}\diamond\boldsymbol{b}$ results in a symmetric matrix. Then, the 10 independent blocks of the Hessian matrix of the rotation angle with respect to the nodal coordinates are expressed as

$$\frac{\partial^2\theta}{\partial(\mathbf{x}_i^{(r)})^2}=-\frac{\|\boldsymbol{r}_{kj}\|}{\|\boldsymbol{m}\|^4}(\boldsymbol{m}\diamond(\boldsymbol{r}_{kj}\times\boldsymbol{m})),\tag{A 10}$$

$$\frac{\partial^2\theta}{\partial(\mathbf{x}_\ell^{(r)})^2}=\frac{\|\boldsymbol{r}_{kj}\|}{\|\boldsymbol{n}\|^4}(\boldsymbol{n}\diamond(\boldsymbol{r}_{kj}\times\boldsymbol{n})),\tag{A 11}$$

$$\frac{\partial^2\theta}{\partial \mathbf{x}_i^{(r)}\mathbf{x}_k^{(r)}} = \frac{\boldsymbol{m}\otimes\boldsymbol{r}_{kj}}{\|\boldsymbol{m}\|^2\|\boldsymbol{r}_{kj}\|} + \frac{\|\boldsymbol{r}_{kj}\|}{\|\boldsymbol{m}\|^4}(\boldsymbol{m}\diamond(\boldsymbol{r}_{ij}\times\boldsymbol{m})), \tag{A 12}$$

$$\frac{\partial^2\theta}{\partial \mathbf{x}_\ell^{(r)}\mathbf{x}_j^{(r)}} = \frac{\boldsymbol{n}\otimes\boldsymbol{r}_{kj}}{\|\boldsymbol{n}\|^2\|\boldsymbol{r}_{kj}\|} - \frac{\|\boldsymbol{r}_{kj}\|}{\|\boldsymbol{n}\|^4}(\boldsymbol{n}\diamond(\boldsymbol{r}_{k\ell}\times\boldsymbol{n})), \tag{A 13}$$

$$\frac{\partial^2\theta}{\partial \mathbf{x}_i^{(r)}\mathbf{x}_j^{(r)}} = -\frac{\boldsymbol{m}\otimes\boldsymbol{r}_{kj}}{\|\boldsymbol{m}\|^2\|\boldsymbol{r}_{kj}\|} + \frac{\|\boldsymbol{r}_{kj}\|}{\|\boldsymbol{m}\|^4}(\boldsymbol{m}\diamond((\boldsymbol{r}_{kj}-\boldsymbol{r}_{ij})\times\boldsymbol{m})), \tag{A 14}$$

$$\frac{\partial^2\theta}{\partial \mathbf{x}_\ell^{(r)}\mathbf{x}_k^{(r)}} = -\frac{\boldsymbol{n}\otimes\boldsymbol{r}_{kj}}{\|\boldsymbol{n}\|^2\|\boldsymbol{r}_{kj}\|} - \frac{\|\boldsymbol{r}_{kj}\|}{\|\boldsymbol{n}\|^4}(\boldsymbol{n}\diamond((\boldsymbol{r}_{kj}-\boldsymbol{r}_{k\ell})\times\boldsymbol{n})), \tag{A 15}$$

$$\frac{\partial^2\theta}{(\partial \mathbf{x}_j^{(r)})^2} = \frac{\partial\theta}{\partial \mathbf{x}_i^{(r)}}\otimes\frac{\partial A}{\partial \mathbf{x}_j^{(r)}} + (A-1)\frac{\partial^2\theta}{\partial \mathbf{x}_i^{(r)}\mathbf{x}_j^{(r)}} - \left(\frac{\partial\theta}{\partial \mathbf{x}_\ell^{(r)}}\otimes\frac{\partial B}{\partial \mathbf{x}_j^{(r)}} + B\frac{\partial^2\theta}{\partial \mathbf{x}_\ell^{(r)}\mathbf{x}_j^{(r)}}\right), \tag{A 16}$$

$$\frac{\partial^2\theta}{\partial \mathbf{x}_j^{(r)}\partial \mathbf{x}_k^{(r)}} = \frac{\partial\theta}{\partial \mathbf{x}_i^{(r)}}\otimes\frac{\partial A}{\partial \mathbf{x}_k^{(r)}} + (A-1)\frac{\partial^2\theta}{\partial \mathbf{x}_i^{(r)}\mathbf{x}_k^{(r)}} - \left(\frac{\partial\theta}{\partial \mathbf{x}_\ell^{(r)}}\otimes\frac{\partial B}{\partial \mathbf{x}_k^{(r)}} + B\frac{\partial^2\theta}{\partial \mathbf{x}_\ell^{(r)}\mathbf{x}_k^{(r)}}\right), \tag{A 17}$$

$$\frac{\partial^2\theta}{(\partial \mathbf{x}_k^{(r)})^2} = \frac{\partial\theta}{\partial \mathbf{x}_\ell^{(r)}}\otimes\frac{\partial B}{\partial \mathbf{x}_k^{(r)}} + (B-1)\frac{\partial^2\theta}{\partial \mathbf{x}_\ell^{(r)}\mathbf{x}_k^{(r)}} - \left(\frac{\partial\theta}{\partial \mathbf{x}_i^{(r)}}\otimes\frac{\partial A}{\partial \mathbf{x}_k^{(r)}} + A\frac{\partial^2\theta}{\partial \mathbf{x}_i^{(r)}\mathbf{x}_k^{(r)}}\right) \tag{A 18}$$

and

$$\frac{\partial^2\theta}{\partial \mathbf{x}_\ell^{(r)}\mathbf{x}_i^{(r)}} = \mathbf{0}_{3\times3}. \tag{A 19}$$

The symbol $\mathbf{0}_{3\times3}$ means a 3×3 zero matrix. Owing to symmetry, the other 6 blocks of the Hessian matrix can be completed with the following identities:

$$\left.\begin{aligned}
&\frac{\partial^2\theta}{\partial \mathbf{x}_k^{(r)}\mathbf{x}_i^{(r)}} = \left(\frac{\partial^2\theta}{\partial \mathbf{x}_i^{(r)}\mathbf{x}_k^{(r)}}\right)^{\mathrm{T}}, \quad \frac{\partial^2\theta}{\partial \mathbf{x}_j^{(r)}\mathbf{x}_\ell^{(r)}} = \left(\frac{\partial^2\theta}{\partial \mathbf{x}_\ell^{(r)}\mathbf{x}_j^{(r)}}\right)^{\mathrm{T}},\\
&\frac{\partial^2\theta}{\partial \mathbf{x}_j^{(r)}\mathbf{x}_i^{(r)}} = \left(\frac{\partial^2\theta}{\partial \mathbf{x}_i^{(r)}\mathbf{x}_j^{(r)}}\right)^{\mathrm{T}}, \frac{\partial^2\theta}{\partial \mathbf{x}_k^{(r)}\mathbf{x}_j^{(r)}} = \left(\frac{\partial^2\theta}{\partial \mathbf{x}_j^{(r)}\mathbf{x}_k^{(r)}}\right)^{\mathrm{T}}\\
\text{and}\quad &\frac{\partial^2\theta}{\partial \mathbf{x}_i^{(r)}\mathbf{x}_\ell^{(r)}} = \left(\frac{\partial^2\theta}{\partial \mathbf{x}_\ell^{(r)}\mathbf{x}_i^{(r)}}\right)^{\mathrm{T}}, \quad \frac{\partial^2\theta}{\partial \mathbf{x}_k^{(r)}\mathbf{x}_\ell^{(r)}} = \left(\frac{\partial^2\theta}{\partial \mathbf{x}_\ell^{(r)}\mathbf{x}_k^{(r)}}\right)^{\mathrm{T}}.
\end{aligned}\right\} \tag{A 20}$$

The terms shown above are not completely simplified, but they are sufficient for numerical computation as they are free of any singularities.

Appendix B. Verification using finite differences

The correctness of the derived terms are verified by the FD method. We take an example of a single rotational spring element (whose geometry is the same as in §4a). Let θ rotate from 0 to 2π. We adopt the central difference formula [44] with a step size of $\delta\theta = 10^{-6}$. In the approximation of the gradient $\nabla\theta$, the dihedral angles are computed using equation (2.27). In the approximation of the Hessian matrix $\mathbf{H}$, the gradient is computed using equations (2.33)–(2.36). The entries of the gradient vector and Hessian matrix are approximated one by one. We define the following measures of differences:

$$\Delta_g = \max_i |(\nabla\theta)_i - (\nabla\theta)_i^{\mathrm{FD}}| \tag{B 1}$$

and

$$\Delta_H = \max_{i,j} |H_{ij} - H_{ij}^{\mathrm{FD}}|, \tag{B 2}$$

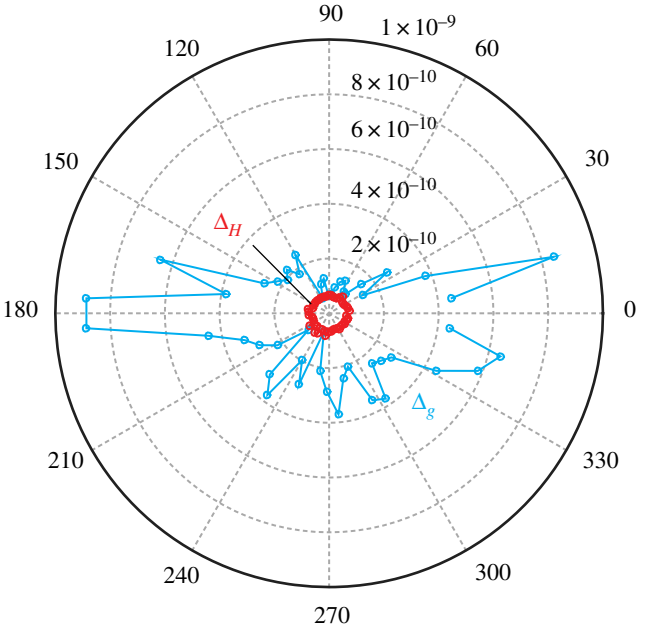

Figure 15. The difference between the analytical expressions and FD approximations versus the rotation angle θ (in degree) for a single rotational spring element—see §4a and figure 7. (Online version in colour.)

where a quantity with superscript FD indicates that it is computed using the finite difference approximation; otherwise, it is computed using the derived analytical formula. The differences are plotted in figure 15 with respect to the dihedral angle θ. Note that due to the ill-conditioning of the inverse cosine function near $\theta = 0$ and π [44], the FD approximations for the gradient become inaccurate near those angles. As a consequence, we find a comparably larger difference between the analytical value and the FD approximation for the gradient near 0 and π than for other angles. In general, the two approaches yield almost identical results for both the gradient and the Hessian, which verifies the correctness of the analytical derivations.

Appendix C. Nomenclature

$\boldsymbol{E}$	Green-Lagrange strain tensor
$\boldsymbol{m}, \boldsymbol{n}$	panel normals
$\boldsymbol{r}_{pq}$	vector from node q to p
$\boldsymbol{S}$	second Piola-Kirchhoff stress tensor
$\Delta\hat{\mathbf{u}}_k^i$, $\Delta\check{\mathbf{u}}_k^i$	intermediate displacement increments
$\Delta\lambda_k^i$	load factor increment at iteration k of increment i
$\Delta L^{(r)}$	change of the axis length
Δ	displacement measure
Δ_g, Δ_h	difference between analytical expressions and FD approximations
η	sign indicator
κ_1, κ_2	principal curvatures
λ	load factor
λ_k^i	load factor at iteration k of increment i
λ_i	principal stretch along direction i
$\mathbf{0}_{3\times3}$	3×3 zero matrix
$\mathbf{B}_1$, $\mathbf{B}_2$	compatibility vector and matrix
$\mathbf{e}_1$	unit vector $[1\,0\,0]^{\mathrm{T}}$

$\mathbf{F}$	applied forces
$\mathbf{H}$	hessian of rotational angle with respect to nodal positions
$\mathbf{I}_{3\times3}$	3-by-3 identity matrix
$\mathbf{K}_{\text{bar}}^{(e)}$	elemental tangent stiffness matrix of a bar element
$\mathbf{K}_{\text{spr}}^{(r)}$	elemental tangent stiffness matrix of a rotational spring element
$\mathbf{R}$	residual force vector
$\mathbf{T}_{\text{bar}}^{(e)}$	internal force vector of a bar element
$\mathbf{T}_{\text{spr}}^{(r)}$	Internal force vector of a rotational spring element
$\mathbf{u}^{(i)}$	nodal displacements
$\mathbf{v}$	admissible virtual displacement
$\mathbf{X}$	undeformed configuration
$\mathbf{x}$	deformed configuration
μ, α, N	Ogden material model parameters
$\nabla\theta$	gradient of rotational angle with respect to nodal positions
ν_{LW}	tangential Poisson's ratio
$\overline{\Delta\lambda}$	initial load factor
Π	total potential energy
ψ	strain energy function of rotational springs
θ	relative rotation angle between two adjacent triangles
$A^{(i)}$	undeformed cross-sectional area of bar i
C, C_0	one dimensional tangent modulus and its initial value
i, j, k, ℓ	nodal indices
k	tangent rotational stiffness
k_0, θ_1, θ_2	parameters for the constitutive model of rotational springs
$k_0^{\text{F}}, k_0^{\text{B}}$	folding stiffness and bending stiffness at neutral state, respectively
L, W	global length and width of a Miura-ori (deformed)
$L^{(i)}$	undeformed length of bar i
$L^{(r)}$	undeformed length of a rotational hinge (axis)
L_{initial}	initial length of the partially folded Miura-ori
L_{unfold}	length of the flat Miura-ori pattern
M	rotational resistance moment
N_a, N_b	linear shape functions of a bar element
U_{bar}	stored energy in bars
U_{spr}	stored energy in rotational springs
V_{ext}	work done by external force
W	strain energy density function of bars

References

1. Lang RJ, Magleby S, Howell LL. 2015 Single-degree-of-freedom rigidly foldable cut origami flashers. *J. Mech. Robot.* **8**, 031005. (doi:10.1115/1.4032102)
2. Wilson L, Pellegrino S, Danner R. 2013 Origami inspired concepts for space telescopes. In *54th AIAA/ASME/ASCE/AHS/ASC Structures, Structural Dynamics, and Materials Conference, Boston, MA, 8–11 April*. Reston, VA: ACAA.
3. Filipov ET, Tachi T, Paulino GH. 2015 Origami tubes assembled into stiff, yet reconfigurable structures and metamaterials. *Proc. Natl Acad. Sci.* **112**, 12 321–123 26. (doi:10.1073/pnas.1509465112)
4. Zhang Y *et al.* 2015 A mechanically driven form of Kirigami as a route to 3D mesostructures in micro/nanomembranes. *Proc. Natl Acad. Sci.* **112**, 11 757–11 764. (doi:10.1073/pnas.1515602112)
5. Schenk M, Guest SD. 2013 Geometry of Miura-folded metamaterials. *Proc. Natl Acad. Sci.* **110**, 3276–3281. (doi:10.1073/pnas.1217998110)

6. Belcastro SM, Hull TC. 2002 Modelling the folding of paper into three dimensions using affine transformations. *Linear Algebra Appl.* **348**, 273–282. (doi:10.1016/S0024-3795(01)00608-5)
7. Tachi T. 2006 Simulation of rigid origami. In *Origami 4* (ed. RJ Lang), pp. 175–187. Boca Raton, FL: A. K. Peters/CRC Press.
8. Wu W, You Z. 2010 Modelling rigid origami with quaternions and dual quaternions. *Proc. R. Soc. A* **466**, 2155–2174. (doi:10.1098/rspa.2009.0625)
9. Gattas JM, Wu W, You Z. 2013 Miura-base rigid origami: parameterizations of first-level derivative and piecewise geometries. *J. Mech. Des.* **135**, 111011. (doi:10.1115/1.4025380)
10. Zhou X, Zang S, You Z. 2016 Origami mechanical metamaterials based on the Miura-derivative fold patterns. *Proc. R. Soc. A* **472**, 20160361. (doi:10.1098/rspa.2016.0361)
11. Reddy JN. 2006 *Theory and analysis of elastic plates and shells*. 2nd edn. Boca Raton, FL: CRC Press.
12. Gattas JM, You Z. 2014 Quasi-static impact of indented foldcores. *Int. J. Impact Eng.* **73**, 15–29. (doi:10.1016/j.ijimpeng.2014.06.001)
13. Gattas JM, You Z. 2015 The behaviour of curved-crease foldcores under low-velocity impact loads. *Int. J. Solids Struct.* **53**, 80–91. (doi:10.1016/j.ijsolstr.2014.10.019)
14. Lv C, Krishnaraju D, Konjevod G, Yu H, Jiang H. 2014 Origami based mechanical metamaterials. *Sci. Rep.* **4**, 1–6. (doi:10.1038/srep05979)
15. Filipov ET, Paulino GH, Tachi T. 2016 Origami tubes with reconfigurable polygonal. *Proc. R. Soc. A* **472**, 20150607. (doi:10.1098/rspa.2015.0607)
16. Hauptmann R, Schweizerhof K. 1998 A systematic development of 'solid-shell' element formulations for linear and non-linear analyses employing only displacement degrees of freedom. *Int. J. Numer. Methods Eng.* **42**, 49–69. (doi:10.1002/(SICI)1097-0207(19980515)42:1<49::AID-NME349>3.0.CO;2-2)
17. Ramm E, Wall WA. 2004 Shell structures: a sensitive interrelation between physics and numerics. *Int. J. Numer. Methods Eng.* **60**, 381–427. (doi:10.1002/nme.967)
18. Lee PS, Noh HC, Bathe KJ. 2007 Insight into 3-node triangular shell finite elements: the effects of element isotropy and mesh patterns. *Comput. Struct.* **85**, 404–418. (doi:10.1016/j.compstruc.2006.10.006)
19. Ota NSN, Wilson L, Pellegrino S, Pimenta PM. 2016 Nonlinear dynamic analysis of creased shells. *Finite Elem. in Anal. Des.* **121**, 64–74. (doi:10.1016/j.finel.2016.07.008)
20. Resch RD, Christiansen H. 1970 The design and analysis of kinematic folded plate systems. In *IASS Symp. on Folded Plates and Prismatic Structures, Vienna, Austria, September/October*, pp. 1–38. Vienna, Austria: Eigentümer.
21. Kumar P, Pellegrino S. 2000 Computation of kinematic paths and bifurcation points. *Int. J. Solids Struct.* **37**, 7003–7027. (doi:10.1016/S0020-7683(99)00327-3)
22. Evans AA, Silverberg JL, Santangelo CD. 2015 Lattice mechanics of origami tessellations. *Phys. Rev. E* **92**, 013205. (doi:10.1103/PhysRevE.92.013205)
23. Tachi T. 2013 Interactive form-finding of elastic Origami. In *Proc. of the Int. Association for Shell and Spatial Structures* (*IASS*) *Symposium, 2013, Wroclaw, Poland, 23–27 September* (eds JB Obrebski, R Tarczewski), pp. 7–10. Madrid, Spain: IASS.
24. Brunck V, Lechenault F, Reid A, Adda-Bedia M. 2016 Elastic theory of origami-based metamaterials. *Phys. Rev. E* **93**, 033005. (doi:10.1103/PhysRevE.93.033005)
25. Schenk M, Guest SD. 2011 Origami folding: a structural engineering approach. In *Origami 5* (eds P Wang-Iverson, RJ Lang, M Yim), pp. 293–305. Boca Raton, FL: CRC Press.
26. Schenk M. 2011 *Folded shell structures* [*Clare College*]. Cambridge, UK: University of Cambridge.
27. Witten TA. 2007 Stress focusing in elastic sheets. *Rev. Modern Phys.* **79**, 643–675. (doi:10.1103/RevModPhys.79.643)
28. Silverberg JL, Evans AA, McLeod L, Hayward RC, Hull T, Santangelo CD, Cohen I. 2014 Using origami design principles to fold reprogrammable mechanical metamaterials. *Science* **345**, 647–650. (doi:10.1126/science.1252876)
29. Wei ZY, Guo ZV, Dudte L, Liang HY, Mahadevan L. 2013 Geometric mechanics of periodic pleated origami. *Phys. Rev. Lett.* **110**, 215501. (doi:10.1103/PhysRevLett.110.215501)
30. Bridson R, Marino S, Fedkiw R. 2003 Simulation of clothing with folds and wrinkles. In *Proc. of the Eurographics/SIGGRAPH Symp. on Computer Animation, San Diego, CA, 26–27 July* (eds D Breen, M Lin), vol. 21, pp. 28–36. Eurographics Association.
31. Guest SD, Pellegrino S. 1996 The folding of triangulated cylinders, Part III: experiments. *ASME J. Appl. Mech.* **63**, 77–83. (doi:10.1115/1.2787212)

32. Fuchi K, Buskohl PR, Bazzan G, Durstock MF, Reich GW, Vaia RA, Joo JJ. 2015 Origami actuator design and networking through crease topology optimization. *J. Mech. Des.* **137**, 091401. (doi:10.1115/1.4030876)
33. Fuchi K, Diaz AR. 2013 Origami design by topology optimization. *J. Mech. Des.* **135**, 111003. (doi:10.1115/1.4025384)
34. Gallagher RH. 1963 Techniques for the derivation of element stiffness matrices. *AIAA J.* **1**, 1431–1432. (doi:10.2514/3.1820)
35. Gallagher RH. 1964 *A correlation study of methods of matrix structural analysis*. Oxford, UK: Pergamon.
36. McGuire W, Gallagher RH, Ziemian RD. 2000 *Matrix structural analysis*, 2nd edn. New York, NY: Wiley.
37. Gallagher RH. 1975 *Finite element analysis: fundamentals*. 1st edn. Englewood Cliffs, NJ: Prentice Hall.
38. Liu K, Paulino GH. 2016 MERLIN: A MATLAB implementation to capture highly nonlinear behavior of non-rigid origami. In *Proc. of the IASS Annual Symp; Spatial Structures in the 21st century, Tokyo, Japan, 26–28 September* (eds K Kawaguchi, M Ohsaki, T Takeuchi). Madrid, Spain: IASS.
39. Bonet J, Wood RD. 2008 *Nonlinear continuum mechanics for finite element analysis*, 2nd edn. Cambridge, UK: Cambridge University Press.
40. Ogden RW. 1997 *Non-linear elastic deformations*. New York, NY: Dover Publications.
41. Wriggers P. 2008 *Nonlinear finite element methods*. Berlin, Germany: Springer.
42. van Schaik RC, Berendsen HJC, Torda AE, van Gunsteren WF. 1993 A structure refinement method based on molecular dynamics in four spatial dimensions. *J. Mol. Biol.* **234**, 751–762. (doi:10.1006/jmbi.1993.1624)
43. Bekker H. 1996 Molecular dynamics simulation methods revised. PhD thesis. University of Groningen, The Netherlands.
44. Heath MT. 1997 *Scientific computing: an introductory survey*. 2nd edn. New York, NY: McGraw-Hill.
45. Ramos Jr AS, Paulino GH. 2015 Convex topology optimization for hyperelastic trusses based on the ground-structure approach. *Struct. Multidiscip. Optim.* **51**, 287–304. (doi:10.1007/s00158-014-1147-2)
46. Crisfield MA. 1996 *Non-linear finite element analysis of solids and structures, volume 1: essentials*. New York, NY: Wiley.
47. Leon SE, Paulino GH, Pereira A, Menezes IFM, Lages EN. 2011 A unified library of nonlinear solution schemes. *Appl. Mech. Rev.* **64**, 040803. (doi:10.1115/1.4006992)
48. Leon SE, Lages EN, de Araújo CN, Paulino GH. 2014 On the effect of constraint parameters on the generalized displacement control method. *Mech. Res. Commun.* **56**, 123–129. (doi:10.1016/j.mechrescom.2013.12.009)
49. Yang YB, Shieh MS. 1990 Solution method for nonlinear problems with multiple critical points. *AIAA J.* **28**, 2110–2116. (doi:10.2514/3.10529)
50. Kresling B. 2008 Natural twist buckling in shells: from the Hawkmoth's bellows to the deployable kresling-pattern and cylindrical Miura-ori. In *Proc. of the 6th Int. Conf. on Computation of Shell and Spatial Structures, Ithaca, NY, 28–31 May* (eds JF Abel, JR Cooke), pp. 1–4.
51. Liu S, Lu G, Chen Y, Leong YW. 2015 Deformation of the Miura-ori patterned sheet. *Int. J. Mech. Sci.* **99**, 130–142. (doi:10.1016/j.ijmecsci.2015.05.009)
52. Smith CW, Wootton RJ, Evans KE. 1999 Interpretation of experimental data for Poisson's ratio of highly nonlinear materials. *Exp. Mech.* **39**, 356–362. (doi:10.1007/BF02329817)
53. Beatty MF, Stalnaker DO. 1986 The Poisson function of finite elasticity. *ASME J. Appl. Mech.* **53**, 807–813. (doi:10.1115/1.3171862)
54. Ting TCT, Chen T. 2005 Poisson's ratio for anisotropic elastic materials can have no bounds. *Q. J. Mech. Appl. Math.* **58**, 73–82. (doi:10.1093/qjmamj/hbh021)
55. Cai J, Deng X, Zhou Y, Feng J, Tu Y. 2015 Bistable behavior of the cylindrical origami structure with Kresling pattern. *J. Mech. Des.* **137**, 061406. (doi:10.1115/1.4030158)
56. Guest SD, Pellegrino S. 1994 The folding of triangulated cylinders, Part I: geometric considerations. *ASME J. Appl. Mech.* **61**, 773–777. (doi:10.1115/1.2901553)
57. Guest SD, Pellegrino S. 1994 The folding of triangulated cylinders, Part II: the folding process. *ASME J. Appl. Mech.* **61**, 778–783. (doi:10.1115/1.2901554)